A Σ-Y two-fluid model with dynamic local topology detection: Application to high-speed droplet impact

Georgia Nykteri[1], Phoevos Koukouvinis[1], Silvestre Roberto Gonzalez Avila[2], Claus-Dieter Ohl[2], Manolis Gavaises[1]

1. School of Mathematics, Computer Science & Engineering, Department of Mechanical Engineering & Aeronautics, City University of London, Northampton Square EC1V 0HB, United Kingdom
2. Institute of Physics, Otto-von-Guericke University Magdeburg, Universitätsplatz 2, 39016 Magdeburg, Germany

Abstract

A numerical methodology resolving flow complexities arising from the coexistence of both multi-scale processes and flow regimes is presented. The methodology employs the compressible Navier-Stokes equations of two interpenetrating fluid media using the two-fluid formulation; this allows for compressibility and slip velocity effects to be considered. On-the-fly criteria switching between a sharp and a diffuse interface within the Eulerian-Eulerian framework along with dynamic interface sharpening is developed, based on an advanced local flow topology detection algorithm. The sharp interface regimes with dimensions larger than the grid size are resolved using the VOF method. For the dispersed flow regime, the methodology incorporates an additional transport equation for the surface-mass fraction (Σ-Y) for estimating the interface surface area between the two phases. To depict the advantages of the proposed multiscale two-fluid approach, a high-speed water droplet impact case has been examined and evaluated against new experimental data; these refer to a millimetre size droplet impacting a solid dry smooth surface at velocity as high as 150m/s, which corresponds to a Weber number of ~7.6×10^5. Droplet splashing is followed by the formation of highly dispersed secondary cloud of droplets, with sizes ranging from 10^{-5}mm close to the wall to less than 1μm forming at the later stages of droplet fragmentation. Additionally, under the investigated impact conditions, compressibility effects dominate the early stages of droplet splashing. A strong shock wave forms and propagates inside the droplet, where transonic Mach numbers occur; local Mach numbers up to 2.5 are observed for the expelled surrounding gas outside the droplet. Relative velocities between the two fluids are also significant; local values on the tip of the injected water film up to 5 times higher than the initial impact velocity are observed. The proposed numerical approach is found to capture relatively accurately the flow phenomena and provide additional information regarding the produced flow structure dimensions, which is not available from the experiment.

Keywords: two-fluid model; compressible Navier-Stokes; Σ-Y formulation; supersonic flow; adaptive flow topology detection; droplet impact

1. Introduction

Multiscale complexities are realised in numerous multiphase flow fields of both industrial and more theoretical interest due to the temporal and spatial geometric diversity of the flow patterns formed by the interacting phases. The different flow structures are characterized by a broad range of scales which as a result, impose the coexistence and dynamic transition between different flow regimes (Kolev, 2007). Examples from the plethora of multidisciplinary applications include fuel spray injection in internal combustion engines, droplet aerodynamic-induced breakup occurring in all type of liquid-fuel combustors (Theofanous, 2011), droplet splashing (Moreira, Moita and Panão, 2010), bubble column bioreactors for chemical processes (Schügerl and Bellgardt, 2000) and even the Rayleigh–Taylor instability in a supernova explosion (Sharp, 1983). With regards to the two-phase flow of a liquid

and a gaseous phase, macroscales dominate the free surface regions, where the two phases are separated with a well-defined interface in the presence of a segregated regime (Ishii and Hibiki, 2011), while flow regions with an intense fluid dispersity due to the dominance of fluid microparticles indicate a dispersed regime (Ishii and Hibiki, 2011). Adding to the complexities imposed by the scale heterogeneity of the flow field, the simultaneous presence of different regimes comes with additional limitations arising from the different physical factors influencing them; surface tension effects dominate the segregated flow, while aerodynamic forces play the dominant role in the dispersed flow regions. Thus, under the scope of a mathematical modelling, it remains challenging and computationally demanding to deal with such multiscale flow systems and simultaneously account for different scaled structures, governed by different physical scales that cannot be captured by the grid resolution available.

Several numerical approaches have been proposed in the literature over the years, regarding the modelling of multiphase flows in engineering applications. Among the most classic models is the Discrete Droplet Method (DDM) (Dukowicz, 1980), in which the dispersed phase is considered as a number of similar physical droplets within a stochastic Lagrangian framework; the conservation equations are solved for the Eulerian continuous phase. Even though the DDM method has been widely utilised in different applications (see selectively (Berlemont, Desjonqueres and Gouesbet, 1990), (Boileau *et al.*, 2008), (Gorokhovski and Saveliev, 2003)), it is generally valid only when the liquid volume fraction is relatively small and the droplets are homogeneously distributed, introducing remarkable limitations in many simulations. In the context of an exclusively Eulerian approach, the homogeneous mixture model (Drew, 1983) is based on the assumption of a single velocity field for both the dispersed and the continuous phases. Due to the simple mathematical formulation and the computational feasibility in liquid fuel spray injection applications under realistic geometries and operating conditions (Koukouvinis *et al.*, 2016), (Pei *et al.*, 2015), the homogeneous mixture model has been implemented and extensively used in both open-source and commercial software. However, the deficiencies regarding the two-phase mixture assumption, the interface diffusivity and the absence of physical sub-grid scale models, often restrict the physical consistency of the obtained results. Under a fully Eulerian formulation, the inhomogeneous mixture model (Ishii and Mishima, 1984), often referred to as the multifluid model, is another alternative approach in which each of the interpenetrating phases is considered separately with a different set of conservation equations; numerical modelling of the mass, momentum and energy exchange mechanisms is required for simulating the interactions between them. Nevertheless, the Eulerian-Eulerian approach provides more accurate results mainly under highly dispersed conditions away from regimes where a dispersed phase cannot be distinguished (Rusche, 2002).

In an attempt to overcome the limitations of the previous models and improve the accuracy of multiphase flow simulations, Direct Numerical Simulations (DNS), which correspond to a full-scale analysis of the local variable topology without any assumptions or additional numerical models introduced, are the optimum numerical tool. However, very few DNS or unresolved-DNS studies can be found in the literature (selectively (Rossinelli *et al.*, 2013), (Gorokhovski and Herrmann, 2008), (Herrmann, 2010), (Shinjo and Umemura, 2010), (Shinjo and Umemura, 2011)), particularly for industrial applications; this is due to the prohibitive computational cost with the current computational capabilities. Focusing specifically on improving the representation of the liquid gas interface, several interface capturing and interface tracking methods have been proposed with the volume of fluid (VOF) method (Hirt and Nichols, 1981), (Scardovelli and Zaleski, 1999), the level-set method (Osher and Fedkiw, 2006), (Sethian, 1996), the ghost-fluid method (Fedkiw *et al.*, 1999) and the front-tracking method (Unverdi and Tryggvason, 1992), (Tryggvason *et al.*, 2002) to be commonly used. A sharp interface approach can be applicable in segregated flows, where large-scale flow

features are dominant and the local interfacial structures can be well resolved under the requirement of a sufficiently fine computational mesh. Thus, an interface sharpening formulation in dispersed flow regions with occurring micro- or even nanoparticles is not computationally feasible.

Recently, more advanced numerical models have been developed in order to overcome the dependency on local flow regimes in specific multiphase flow applications. The ELSA model (Vallet, Burluka and Borghi, 2001) is based on the principles of the Σ-Y model (Vallet and Borghi, 1999), which was initially proposed for simulating the flame surface area evolution in combustion simulations (Marble and Broadwell, 1977); it provides a dynamic transition between a Eulerian and a Lagrangian framework in the primary and secondary liquid spray atomization regions, respectively. The additional transport equation for the liquid gas interface surface area density (Σ) allows for representation of unresolvable sub-grid scale structures with a viable computational cost, ought to the physical modelling of the mechanisms responsible for the interface surface area density formation (Lebas *et al.*, 2009). Several variations and improvements of the original ELSA model have been proposed so far, including vaporisation (Lebas *et al.*, 2009) and slip-velocity effects (Andreini *et al.*, 2016), as well as a sharp interface formulation in the Eulerian part of an atomizing spray (Anez *et al.*, 2018). A further insight into the sub-grid scale phenomena can be gained with the implementation of a probability density function (PDF) so as to obtain secondary droplet size distributions and other stochastic properties of the dilute spray using the Method of Moments (Marchisio *et al.*, 2003), (Marchisio *et al.*, 2003). In one of the most recent formulations, a joint sub-grid scale volume surface PDF (Navarro-Martinez, 2014) is introduced for the liquid surface and volume dependence to predict in more detail the interface surface area density production and destruction at sub-grid level within the ELSA model (Vallet, Burluka and Borghi, 2001). With respect to commercial CFD codes, a complete atomization model for liquid fuel spray simulations has been integrated in AVL FIRE® (AVL, 2013), using a fully Eulerian formulation. The interacting phases are resolved with the incorporation of a specific number of Eulerian droplet classes, which share the same properties (Vujanović *et al.*, 2015). Moreover, in the recent versions of OpenFOAM®, a hybrid fully Eulerian incompressible solver has been implemented, namely multiphaseEulerFoam (Wardle and Weller, 2013) and used in multiscale vertical plunging jets (Shonibare and Wardle, 2015), supporting a dynamic switching between a diffuse and a sharp interface approach within the same multifluid framework. However, the advantages of the state-of-the-art numerical models over the more classic approaches are restricted to the needs of the specific applications for which they were developed. Therefore, there is a gap in the literature for a holistic numerical approach, which can be applicable in any flow field governed by a multiscale character and complex physical phenomena, including high compressibility and slip velocity effects, regardless of the limitations of local flow characteristics.

The above methodologies can be applied to the case of a droplet impacting on solid surfaces, which represents a fundamental multiscale flow problem, that still attracts the scientific interest, due to its relevance in many engineering applications, such as cooling, coating, inkjet printing, fuel injection in internal combustion engines, as it is stated in the review works of (Kandlikar and Bapat, 2007), (Moreira, Moita and Panão, 2010). The droplet deformation and potential fragmentation after impact is very sensitive to several parameters regarding the impact and target conditions; namely the impact velocity, the droplet initial diameter and physical properties, target wettability, roughness and surface temperature, as it has been investigated in numerous experimental studies (see selectively (Pan, Tseng and Wang, 2010), (Visser *et al.*, 2012), (Antonini, Amirfazli and Marengo, 2012), (Roisman, Lembach and Tropea, 2015), (Liang and Mudawar, 2017)). The post-impact outcomes are subject to different regimes, ranging from spreading or even sticking on the surface to rebounding and splashing and they have been comprehensively presented in the literature (Rein, 1993), (Yarin, 2006), (Josserand and Thoroddsen, 2016) and illustrated on regime maps as a function of dimensionless impact

parameters (Ma *et al.*, 2017), (Bertola, 2015). Several correlations to define the splashing regime threshold have been established (Yarin and Weiss, 1995), (Range and Feuillebois, 1998), while the most widely used criterion for the transition between the deposition and splashing regimes under large impact velocities is the parameter of Mundo (Mundo, Sommerfeld and Tropea, 1995), which is based on the Weber and Ohnesorge numbers. Additionally, conducted experimental studies have been utilised for the development of empirical models, corresponding to the droplet post-impact characteristics under the influence of different impact regimes, as it is thoroughly described in (Cossali, Santini and Marengo, 2005), in order to provide numerical models for spray impingement simulations.

Even though the single droplet impact onto solid surfaces has been extensively investigated with experimental studies since 1877 (Worthington, 1877), the mechanisms of the prompt and violent splashing under high impact velocities, which correspond to the massive spatial dispersion of the produced secondary droplets far away from the solid surface and the dominance of compressibility phenomena with strong propagating shock waves inside the deforming droplet, have not been precisely revealed yet. Due to the limitation of the high speeds and small structures involved, recent advancements in imaging technologies (Thoroddsen, Etoh and Takehara, 2008) have contributed to the performance of new experiments under higher impact velocities. In (Xu, Zhang and Nagel, 2005) the corona splashing of an ethanol droplet on a dry and smooth surface with impact Weber number equal to 1685 was examined; the created lamella reached a maximum spreading velocity of 30m/s. In (Visser *et al.*, 2015) experiments with water microdroplets have been conducted, impacting on both hydrophilic and hydrophobic surfaces with velocities up to 50m/s and Weber numbers that do not exceed the value of 1770. However, despite the high speed conditions, no splash but only spreading of the droplet on the surface was observed, due to the influence of the surrounding air. One of the few and most recent experiments in which a prompt splashing was illustrated is the work of (Thoroddsen, Takehara and Etoh, 2012), in which a water droplet was subject to an impact with a smooth and solid surface at Weber numbers up to 2480, followed by the creation of water microdroplets with maximum spreading velocity of 100m/s. Finally, in (Field, Dear and Ogren, 1989) an experiment of high speed droplet impact at 110m/s was performed, with emphasis put on capturing the propagating shock wave inside the droplet at the early stages of the impact with the target, without examining the later splashing effects. Thus, it is noticeable from the literature that high-speed droplet impact experiments are limited; available studies do not exceed Weber number values of 2500 and they mainly focus on the early stages of the droplet and wall interaction.

Regarding the numerical investigation of droplet impact cases, most recent studies examine the impact on solid surfaces under the spreading (Malgarinos *et al.*, 2014), (Visser *et al.*, 2015) or the corona splashing (Guo, Lian and Sussman, 2016), (Wu and Cao, 2017) regimes; they utilise an interface capturing method for the conducted simulations. With the VOF method to be the most commonly used approach, the droplet deformation and spreading on the target can be captured in detail with a sufficiently fine mesh. However, in the case of higher impact velocities, which result to splashing and fragmentation of the droplet into secondary microscale structures, the performed simulations are restricted to the early stages of the phenomena since the later stages of droplet fragmentation are dominated by computationally prohibitive scales for a VOF simulation. Thus, a more advanced numerical modelling is required to deal simultaneously with the early and later stages of the splashing droplet evolution. Moreover, other studies perform high-speed droplet impact simulations with the focus on capturing the occurring compressibility phenomena (Haller *et al.*, 2002), (Niu and Wang, 2016), (Kyriazis, Koukouvinis and Gavaises, 2018), (Wu, Xiang and Wang, 2018) namely the strong shock waves inside the droplet and the produced cavitation regions, which are formed and dominate during the early stages of the impact, excluding in this manner the secondary droplet dispersion from the scope of their numerical investigation.

Following the limitations of the currently used numerical methodologies in multiscale flow applications, the present study proposes a new numerical framework which has been developed in OpenFOAM® utilising the two-fluid formulation (Ishii and Mishima, 1984); this allows for both compressibility and slip velocity effects to be taken into account. The model solves for an additional transport equation for the interface surface area density; the previously developed Σ-Y model (Vallet and Borghi, 1999) for incompressible flows is coupled here for the first time with a compressible two-fluid framework. This provides significant information for the unresolved sub-grid scale phenomena, which are related to the interface formation during the flow development. The Σ-Y two-fluid model is also combined with a dynamic switching between the sharp and the diffuse interface approaches that co-exist during the numerical solution at different parts of the computational domain. Thus, it is possible to deal simultaneously with the segregated and the dispersed flow regions; the two-fluid model formulation has been coupled with the VOF method to operate under the segregated flow regime. The dynamic switching is performed with an advanced topology detection algorithm relative to criteria available in the literature (Wardle and Weller, 2013), (Anez *et al.*, 2018). However, apart from the numerical limitations of the VOF and the diffuse interface approaches with respect to the computational mesh which correspond to the commonly used switching criteria, the proposed flow topology detection algorithm also evaluates the local flow characteristics. The developed methodology is initially validated against a shock tube problem and a rising bubble. Following, validation is performed against the challenging case of a high-speed droplet impact, using new experimental data obtained specifically for this case. These refer to impact Weber number of the order of 10^5, which is much higher than the available up-to-date literature. Finally, emphasis from the numerical perspective is given on providing an insight into the dispersed regions of the flow field at the later stages of the droplet fragmentation evolution, where even the experimental investigation cannot contribute with sufficient information due to limitations in diagnostic methods for high Mach number flows consisting of a large number of droplets with sizes less than 1μm.

2. Numerical Model

The Σ-Y two-fluid model with dynamic local topology detection has been implemented in OpenFOAM® with further developments on twoPhaseEulerFoam solver, an available compressible Eulerian pressure-based solver. In principle, the numerical model consists of the same set of governing equations for both multiscale formulations, namely the sharp and the diffuse interface approach, with specific source terms to be activated and deactivated depending on the currently operating formulation of the solver, as it is described in detail below.

2.1. Two-Fluid Model Governing Equations

In the context of a two-fluid approach (Ishii and Mishima, 1984), the volume averaged conservation equations governing the balance of mass, momentum and energy are solved separately for each phase k:

$$\frac{\partial}{\partial t}(a_k\rho_k) + \nabla\cdot(a_k\rho_k u_k) = 0 \tag{1}$$

$$\frac{\partial}{\partial t}(a_k\rho_k u_k) + \nabla\cdot(a_k\rho_k u_k u_k) = -a_k\nabla p + \nabla\cdot\left(a_k\boldsymbol{\tau}_k^{eff}\right) + a_k\rho_k g + \sum_{\substack{n=1\\n\neq k}}^{2} M_{kn} \tag{2}$$

$$\frac{\partial}{\partial t}[a_k\rho_k(e_k+k_k)] + \nabla\cdot[a_k\rho_k(e_k+k_k)u_k] = -\nabla\cdot\left(a_k\boldsymbol{q}_k^{eff}\right) - \left[\frac{\partial a_k}{\partial t}p + \nabla\cdot(a_k u_k p)\right] + a_k\rho_k g\cdot u_k + \sum_{\substack{n=1\\n\neq k}}^{2} E_{kn} \tag{3}$$

The numerical method is based on a finite-volume framework, using an implicit pressure-based solver for the governing equations of the two-fluid model. Numerical coupling for the independent systems of conservation equations is achieved through additional source terms added to the Navier-Stokes equations, which appear after the imposed averaging procedure. These source terms account for the mass, momentum and energy exchange phenomena by providing suitable closure relations for the macroscopic interfacial interactions occurring in a transient multiphase flow system. Specifically, the interfacial momentum source term M_{kn} represents the forces acting on the dispersed phase and depends on local topology, since different forces are dominant under different flow regimes. The interfacial energy source term E_{kn} demonstrates the heat transfer between the phases that can be modelled via a standard heat transfer law. The interfacial mass source term, which is responsible for the mass transfer due to phase-change effects or other interfacial phenomena that result to production or destruction of the interface, such as sub-grid scale turbulence and droplet interactions, is not implemented in the continuity equations as expected. Instead, in the present work the mass exchange contributions with an effect on interface formation are considered in the transport equation for the liquid gas interface surface area density. Phase-change phenomena, like vaporisation and cavitation, are neglected since they are negligible in the examined high-speed droplet impact case at the early stages of impact, where temperature variation around the standard conditions is not significant and local pressure drop is not sufficient to cause remarkable cavitation regions, as it has been stated before in the literature for similar impact conditions (Niu and Wang, 2016), (Kyriazis, Koukouvinis and Gavaises, 2018).

Viscous and turbulence effects are introduced in the model with the effective stress tensor $\boldsymbol{\tau}^{eff}$ in the momentum equations and the effective heat flux vector $\mathbf{q}^{eff}$ in the energy equations; $\boldsymbol{\tau}^{eff}$ accounts for the molecular viscosity and the Reynolds stress tensor, which based on Boussinesq's hypothesis relates turbulent velocity fluctuations to the eddy viscosity (Boussinesq, 1877); $\mathbf{q}^{eff}$ corresponds to the laminar and turbulent thermal diffusivity. For the turbulent components, appropriate models are implemented within either a RANS or an LES framework in OpenFOAM®; LES modelling is used for the turbulent flow cases in the present study with the implementation of the one-equation SGS model (Lahey, 2005). Given the occurring Reynolds numbers, a dimensionless wall distance y^+ with a value lower 1 is observed; thus, the appropriate turbulent wall functions are implemented for capturing the near-wall phenomena; the two-layer wall function is used which is a blending between the logarithmic and the linear laws for the turbulent and viscous sublayers, respectively.

Finally, the thermodynamic closure of the system is achieved by solving independently an individual equation of state for each phase from which the corresponding density field is obtained. In the following simulations, the ideal gas equation of state is used for the gaseous phase and the stiffened gas equation of state (Ivings, Causon and Toro, 1998) has been implemented and used for the liquid phase. The stiffened gas equation of state is basically the same as the ideal gas equation of state with an additional pre-pressurization term to match the density and stiffness of the liquid. Despite its deficiencies, it is commonly used in fundamental studies (Saurel, Petitpas and Abgrall, 2008) and highly violent phenomena (Beig, Aboulhasanzadeh and Johnsen, 2018); moreover, it is known to be valid for the pressure and temperature conditions examined here.

Σ-Y Model Transport Equations:

The liquid dispersion in a liquid and gaseous flow is simulated with the liquid phase volume fraction transport equation, which represents the volume proportion of liquid at a given volume in the computational domain. The transport equation for the liquid volume fraction in a compressible two-phase flow is:

$$\frac{\partial a_l}{\partial t} + \nabla \cdot (a_l u_m) + v_{topo}[\nabla \cdot (a_l(1-a_l)u_c)] = a_l a_g \left(\frac{\psi_g}{\rho_g} - \frac{\psi_l}{\rho_l}\right)\frac{Dp}{Dt} + a_l \nabla \cdot u_m - \left(1 - v_{topo}\right)R_{a_l} \quad (4)$$

where the topological parameter v_{topo} allows for distinguishing between the two different interface approaches by taking either 0 or 1 value under a diffuse or sharp interface formulation respectively. u_c is the artificial compression velocity (Deshpande, Anumolu and Trujillo, 2012) that is introduced along the interface as a countereffect of the inevitable numerical diffusion in order to maintain interface sharpness in flow regions subject to a segregated regime. The turbulent liquid flux $R_{\alpha l}$ (Vallet, Burluka and Borghi, 2001) on the RHS of the transport equation accounts for the liquid dispersion induced by turbulent velocity fluctuations, which is important in dispersed flows and smaller scales. Additionally, since a compressible flow is involved, the gradients of liquid density that are related to compressibility effects on the liquid volume fraction are taken into consideration (Jadidi *et al.*, 2014).

The liquid gas interface surface area density, namely the surface area of the liquid gas interface per unit of volume, provides supplementary information regarding the interface formation without the assumption of a particular shape in the produced flow features. The transport equation for the liquid gas interface surface area density (Lebas *et al.*, 2009) is described as follows:

$$\frac{\partial \Sigma'}{\partial t} + \nabla(\Sigma' u_m) = (1 - v_{topo})\left[-R_\Sigma + C_{SGS}\frac{\Sigma}{\tau_{SGS}}\left(1 - \frac{\Sigma}{\Sigma^*_{SGS}}\right)\right] \quad (5)$$

The turbulent flux of the interface surface area density R_Σ, namely the first source term on the RHS of the transport equation, represents the surface area diffusion due to turbulent velocity fluctuations. The second source term on the RHS accounts for all physical mechanisms which fall below the computational mesh resolution and are responsible for the surface area production and destruction. In sharp interface regions with dominant large scale features the evolution of the interface surface area is captured directly by the computational model and grid. On the contrary, in highly diluted and dispersed flows, the interface production and destruction at sub-grid level affects significantly the overall interface formation; thus, appropriate modelling is required to obtain this sub-grid scale information. Under the assumption of a minimum interface surface area due to simultaneous existence of liquid and gas on the interface (Chesnel *et al.*, 2011), the total interface surface area density is defined as:

$$\Sigma = \Sigma' + \Sigma_{min} \quad (6)$$

where Σ_{min} is the minimum interface surface area density that can be found within a control volume for a given liquid volume fraction value with $0<\alpha_l<1$, which imposes the present of two phases and thus, the presence of an interface in the examined control volume. Based on empirical correlations obtained from CDNS studies and under the assumption of a spherical droplet inside the examined computational cell, Σ_{min} is defined as $\Sigma_{min} = 2.4\sqrt{a_l(1-a_l)}V_{sphere}^{-1/3}$ (Chesnel *et al.*, 2011).

2.2. Sharp Interface Approach

Interface sharpening is implemented in OpenFOAM® with the MULES algorithm (Deshpande, Anumolu and Trujillo, 2012), an iterative technique which guarantees boundness of the volume fraction and sharpness at the interface by modifying the advection term in the transport equation for the volume fraction. In this manner, an additional advection term is introduced which acts as an artificial compression in order to maintain sharpness without the need for interface reconstruction. This approach has been implemented within the proposed multiscale two-fluid framework and thus in the segregated flow regions the transport equation for the liquid volume fraction takes the final form of

equation (4) with the topological parameter v_{topo} set to 1. Then, the artificial compression velocity u_c is given by the expression:

$$u_c = C_a |u_m| \frac{\nabla a_l}{|\nabla a_l|} \tag{7}$$

with C_α the interface compression parameter that takes values equal or greater than 1 so as to increase the imposed interface sharpness. In the following simulations the typical value of C_α=1 has been implemented so as to introduce interface sharpness with the MULES algorithm.

However, the introduction of an interface sharpening approach within a two-fluid framework requires further modifications in the numerical model. In the limit of a sharp interface, the velocities on either side of the interface must be equal in order to eliminate the relative velocity and meet the no-slip interface condition. At the same time, a fundamental principle of the two-fluid model is the presence of separate velocity fields for the two interpenetrating liquids. Several studies in the literature (Černe, Petelin and Tiselj, 2001), (Wardle and Weller, 2013), (Strubelj and Tiselj, 2011) are dealing with the coupling of a two-fluid model and an interface sharpening method by implementing an additional source term in the momentum equations. This extra term practically imposes large interfacial drag values; as a result, the relative velocity on the interface is eliminated and finally the coupling between the two-fluid model and the sharp interface approach is stabilized. In the present model the source term introduced in the momentum equations (2) has an expression similar to the aerodynamic drag force (Strubelj and Tiselj, 2011) and enforces instantaneous equalizing of the velocities near the resolved interface. The artificial drag force is defined as:

$$F_{Da} = v_{topo}\, F(u_r) \frac{\tau_r}{\Delta t} \tag{8}$$

where $F(u_r)$ is an expression proportional to the relative velocity u_r between the two phases and the density of the two-fluid mixture ρ_m with $F(u_r) = a_l(1 - a_l) u_r \rho_m$ as proposed by (Strubelj and Tiselj, 2011), Δt the computational time step and τ_r a relaxation factor which needs to be calibrated correspondingly, in order to meet the no-slip interface condition. As it is described in detail in paragraph 3.2, the elimination of the interfacial relative velocity, which practically results to a stronger coupling between the two-fluid model and the sharp interface approach, is achieved by maximizing the relaxation factor τ_r. In an attempt to avoid any case-dependent calibration of τ_r, an on-the-fly algorithm has been developed which gradually increases the value of τ_r starting from the value of 1, until the point that the tangential component of the relative velocity on the interface reaches a sufficiently low lower-bound close to zero; under this condition, the no-slip interface condition is satisfied. In practice, a numerical criterion is examined on the interface, which requires for the tangential component of the relative velocity to be only a small proportion of the total local relative velocity, approaching a zero value.

Under a segregated flow regime, the surface tension plays a greater role against the aerodynamic forces. Therefore, its contribution should be taken into consideration and a surface tension force is added as a source term in the momentum equations (2). The surface tension force is defined by the Continuum Surface Force (CSF) (Brackbill, Kothe and Zemach, 1992) as:

$$F_s = v_{topo}\, \sigma \kappa \frac{\nabla \rho}{[\rho]} \frac{\rho}{\langle \rho \rangle} \tag{9}$$

where σ is the surface tension coefficient, κ the interface curvature, [ρ] the density jump described as $[\rho]=\rho_g-\rho_l$ and $\langle\rho\rangle$ the density at the interface given by $\langle\rho\rangle=½(\rho_l+\rho_g)$ in order to replace the local discontinuity with a smooth variation.

Regarding the interface density, all sub-grid scale phenomena, which are modelled via source terms in equation (5), are out of the scope of a sharp interface approach and thus, the RHS of the transport equation is set to zero. Besides, a basic principle of the multiscale formulation is the accurate topological distinction between different flow regimes and the imposition of a sharp interface approach in regions where all present flow features can be resolved by the grid resolution used.

2.3. Diffuse Interface Approach

Under a dispersed flow regime with prevailing small dispersed structures, the aerodynamic forces and particularly the drag force acting on the dispersed phase is the dominant factor in interfacial momentum exchange between the liquid and gaseous phases. Different drag models are implemented depending on local flow conditions (Marschall, 2011), i.e. dispersed droplets in continuous gas or dispersed bubbles in continuous liquid. The drag force, which is introduced as the interfacial momentum source term in momentum equations (2), is described as:

$$F_D = (1 - v_{topo})\frac{1}{2}C_D\rho_{continuous}u_r|u_r|A_{particle} \tag{10}$$

where $\rho_{coninuous}$ is the density of the phase, which is considered continuous and $A_{particle}$ is the projected area of a typical dispersed particle. For the estimation of the drag coefficient C_D, there are many empirical models in the literature (Schiller and Naumann, 1933), (Ishii and Zuber, 1979), (Tomiyama and Shimada, 2001) depending on properties of the flow field and the discrete particle characteristics. In the present work, where the focus is mainly on the motion of very small droplets in highly dispersed flows with low or moderate Reynolds numbers, C_D is obtained from the model of Rodi and Fueyo (Kelbaliyev, 2011):

$$C_D = \begin{cases} \frac{16}{Re}, & Re < 1.5 \\ \frac{14.9}{Re^{0.78}}, & 1.5 < Re \leq 80 \\ \frac{49.9}{Re}\left(1 - \frac{2.21}{Re^{0.5}}\right) + 1.17 \times 10^{-8}Re^{2.615}, & 80 < Re \leq 1530 \\ 2.61, & Re > 1530 \end{cases} \tag{11}$$

However, since many semi-empirical correlations are involved, the closure relations of the interfacial source terms are usually the main cause for the uncertainties of the two-fluid model. In an attempt to reduce the possible inaccuracies, in the proposed numerical model the interface surface area is obtained from the transport equation for the interface surface area density, which is used to calculate a characteristic length corresponding to the flow structures in each computational cell. More specifically, the diameter of a spherical particle which has the same volume to surface area ratio as the examined computational cell volume to the calculated interface surface area density, is used as the equivalent dispersed particle diameter in drag force calculations. Then, the interface surface area density diameter can be defined as follows (Chesnel *et al.*, 2011):

$$d_\Sigma = \frac{6a_l(1-a_l)}{\Sigma} \tag{12}$$

Concerning the transport equation for the liquid volume fraction, the diffuse interface approach results to exclusion of the interface compression term; consideration of the sub-grid turbulent fluctuations, as it appears in equation (4) with the topological parameter v_{topo}, is set to 0. The turbulent liquid flux $R_{\alpha l}$ (Vallet, Burluka and Borghi, 2001) on the RHS of the transport equation represents stochastic liquid dispersion phenomena due to the occurring turbulence. Previous studies on modelling $R_{\alpha l}$ (Demoulin *et al.*, 2007), (Andreini *et al.*, 2016) depict a relation between the statistically dependent turbulent velocity fluctuations and the averaged local relative velocity, which corresponds to a correlation between slip and drift velocities of the mean flow field, as presented below:

$$R_{a_l} = -\nabla \cdot \left(\widetilde{a_l'' \rho_l'' u_m''}\right) = -\nabla \cdot [a_l(1-a_l)\rho_l V_r\,] = -\nabla \cdot [a_l(1-a_l)\rho_l(u_r - V_D\,)] \tag{13}$$

where V_r is the local relative velocity, u_r the slip velocity and V_D the drift velocity. The slip velocity contribution to the turbulent liquid flux can be calculated directly without the need of modelling due to the two-fluid formulation. As for the drift velocity effects, they are modelled via a first order closure (García-Oliver *et al.*, 2013), namely a classic gradient law using the turbulent properties of the liquid and gaseous mixture.

A significant advantage of the proposed multiscale two-fluid formulation is the coupling with the transport equation for the interface surface area density. Especially within the framework of a diffuse interface approach, where the interface is neither tracked nor resolved by the grid resolution, this additional information provides an insight into the interface surface area density evolution in space and time even in the sub-grid scales. Examining the source terms on the RHS of equation (5), which are activated under the dispersed regime, the turbulent flux of the interface surface area density R_Σ accounts for its dispersion due to turbulence. Analogous to the turbulent liquid flux $R_{\alpha l}$ on the RHS of equation (4), R_Σ is a turbulent diffusion term. Then, with respect to the closure of the turbulent liquid flux $R_{\alpha l}$ in equation (13), the turbulent diffusion flux R_Σ is modelled accordingly (Andreini *et al.*, 2016):

$$R_\Sigma = -\nabla \cdot \left(\widetilde{\Sigma' u_m''}\right) = -\nabla \cdot [\Sigma\, a_l(1-a_l)(u_r - V_D\,)] \tag{14}$$

The last term on the RHS of equation (5) represents the sub-grid scale mass exchange phenomena between the liquid and gaseous phases, which have been neglected from the continuity equations (1) and are related to the interface surface area density production and destruction. Different physical mechanisms with an effect on interface formation are included and described by their characteristic time scale τ_{SGS}, the critical interface surface area density Σ^*_{SGS} at an equilibrium state between production and destruction of the interface and an adjustable constant coefficient C_{SGS} set to 1 in the presented cases. In the proposed model, the contributions of turbulent flow stretching and wrinkling particularly in dense flow regions, the droplet collision and coalescence effects, as well as the secondary breakup effects of produced droplets are taken into account with the appropriate closure relations (Lebas *et al.*, 2009) and the implementation of their characteristic time scales τ_{SGS}, which correspond to the Kolmogorov time scale, the collision time scale obtained from the particle collision theory and the breakup time scale based on the droplet Weber number, respectively, to be summarized in Table 1.

Table 1 Closure relations for the SGS terms in equation (5) related to interface surface area production and destruction.

SGS mechanism	τ_{SGS}	Σ^*_{SGS}
turbulence	$\frac{k}{\varepsilon}$	$\frac{\alpha_l(1-\alpha_l)\rho_m k_m}{\sigma We^*_{turb}}$ with $We^*_{turb} = 1$ at equilibrium
collision/coalescence	$\frac{1}{\Sigma\sqrt{\frac{2}{3}k_m}}$	$\frac{6\alpha_l(1-\alpha_l)}{d^*_\Sigma}$ with $d^*_\Sigma = d_\Sigma \frac{1+\frac{We^N_{coll}}{6}}{1+\frac{We_{coll}}{6}}$ • critical We for coalescence: $We^N_{coll} = 12$ • relevant We for collision: $We_{coll} = \frac{4\alpha_l(1-\alpha_l)\rho_l k_m}{\sigma\Sigma}$
secondary breakup	$f(We_{BU})\frac{d_\Sigma}{u_r}\sqrt{\frac{\rho_l}{\rho_g}}$ with $We_{BU} = \frac{6\rho_g u_r^2 \alpha_l(1-\alpha_l)}{\sigma\Sigma}$	$\frac{6\rho_g u_r^2 \alpha_l(1-\alpha_l)}{\sigma We^*_{BU}}$ with $We^*_{BU} = 12(1+1.077Oh^{1.6}) \cong 12$ for Oh <<

2.4. Flow Topology Detection Algorithm

A key factor for the accurate functioning of the multiscale formulation is the implementation of a stable topology detection methodology. The developed algorithm can detect instantaneous topological changes in flow regimes, evaluate the most appropriate numerical treatment for local interfaces and allow for a flexible two-way switching between sharp and diffuse interface approaches. The switching criteria, described in detail below, are applied exclusively in interfacial flow regions as in single phase regions a sharp interface is defined by default.

2.4.1. Switching criterion from sharp to diffuse interface approach

In any computational cell under the sharp interface approach, a diameter of an equivalent spherical structure based on the curvature of the interface can be calculated as (Shonibare and Wardle, 2015):

$$d_{curv} = \frac{2}{\kappa} \tag{15}$$

Assuming that at least 3 computational cells are needed for the grid resolution to capture any spherical structure with sufficient sharpness (Shonibare and Wardle, 2015), the following geometric criterion can be proposed as the limit for the sharp interface approach:

$$d_{curv} < 3 * max\ (d_{cell}) \tag{16}$$

Nevertheless, this geometric criterion can only be considered as an indication for a potential switch to a diffuse interface approach. All computational cells which meet criterion (16) are subject to a second stage of topological examination based on the condition of their neighbour cells. The three different possibilities are as follows:

- A single cell which is supposed to follow a diffuse interface approach based on the geometric criterion but belongs to a strictly segregated region with sharp interfaces, will remain unaffected by changes, as shown in Figure 1(a).
- When a cell is part of a topologically unstable region, where all its neighbour cells previously respected a sharp interface approach but now some of them are also subject to changes, then as depicted in Figure 1(b), an expanded region is examined. Specifically, the surrounding area of the neighbour cells which are of particular interest is evaluated with regards to the occurring topological conditions. Finally, if the examined cell belongs to a highly transitional region, then the topological criterion is met and a change for the interface approach is applied.
- As illustrated in Figure 1(c), any cell that is in the border of transition between segregated and highly dispersed flow regimes will follow the tendency of local interface formation and will be subject to the diffuse interface approach in the following time step.

2.4.2. Switching criterion from diffuse to sharp interface approach

The reset of a sharp interface approach for a previously diffuse cell is performed after meeting a single geometric criterion, which correlates the interface surface area density diameter from equation (12) to the local computational mesh resolution. When the calculated diameter d_Σ is larger than the cell size, then the presumed dispersed flow features can no longer be treated as mesh unresolvable structures and a switch to a sharpened interface state is required.

$$d_\Sigma > min\ (d_{cell}) \tag{17}$$

Since the overall concept of the diffuse interface approach is inextricably linked to sub-grid scale structures, the described geometric criterion is sufficient for changing the interface formulation without examining the surrounding flow conditions, as shown in Figure 1(d).

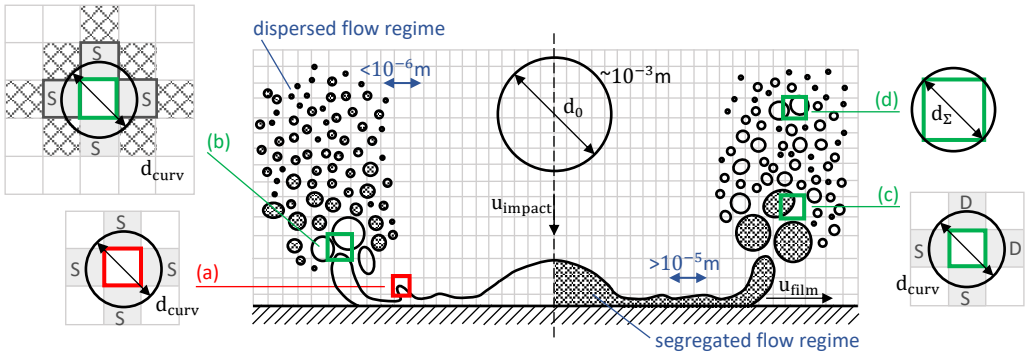

Figure 1 Local topology detection and distinction criteria between the segregated and the dispersed flow regimes in order to impose the appropriate interface approach in each time step. Application in the multiscale flow of a droplet impact on a rigid wall with indicative dominant scales under each flow regime.

3. Results and Discussion

3.1. Two-Phase Shock Tube Problem

Initially, the capability of the proposed compressible two-fluid model to capture accurately the wave dynamics under high density ratios between the interacting phases is examined against the benchmark case of a two-phase shock tube. A one-dimensional 1m long two-fluid shock tube without mass transfer and initial discontinuity at x=0.75m, as studied by (Saurel, Petitpas and Abgrall, 2008), is used for validation. The left part of the shock tube is occupied by liquid dodecane at high pressure $p_l=10^8$Pa and density $\rho_l=500$kg/m^3, while the right part is set at atmospheric conditions with the occurring vapour dodecane at density $\rho_v=2$kg/m^3. The simulation is performed using the twoPhaseEulerFoam solver in a uniform computational grid of 1000, 10000 and 20000 cells with second order spatial accuracy and an adaptive time step to meet the convective Courant–Friedrichs–Lewy (CFL) number of 0.2. As a matter of consistency between the conducted simulation and the results of (Saurel, Petitpas and Abgrall, 2008) using the hyperbolic two-fluid model with two temperature and entropy fields but a single pressure and velocity field, the stiffened gas equation of state with the exact parameters utilised in (Saurel, Petitpas and Abgrall, 2008) has been implemented in OpenFOAM® and applied for the thermodynamic closure. In Figure 2 the results obtained from the proposed two-fluid approach and the model of (Saurel, Petitpas and Abgrall, 2008) are compared with the exact solution at 473μs after the initial contact discontinuity was removed. The involved convectional waves, namely the left-facing rarefaction wave propagating through the liquid dodecane, the moving from left to right contact discontinuity and the right-facing shock wave propagating though the vapour dodecane are accurately captured with the proposed two-fluid model. Moreover, the increase in mesh resolution eliminates the numerical diffusion in the pressure and mixture velocity fields and the illustrated results using the finest mesh converge to a satisfactory agreement with the exact solution of the shock tube problem.

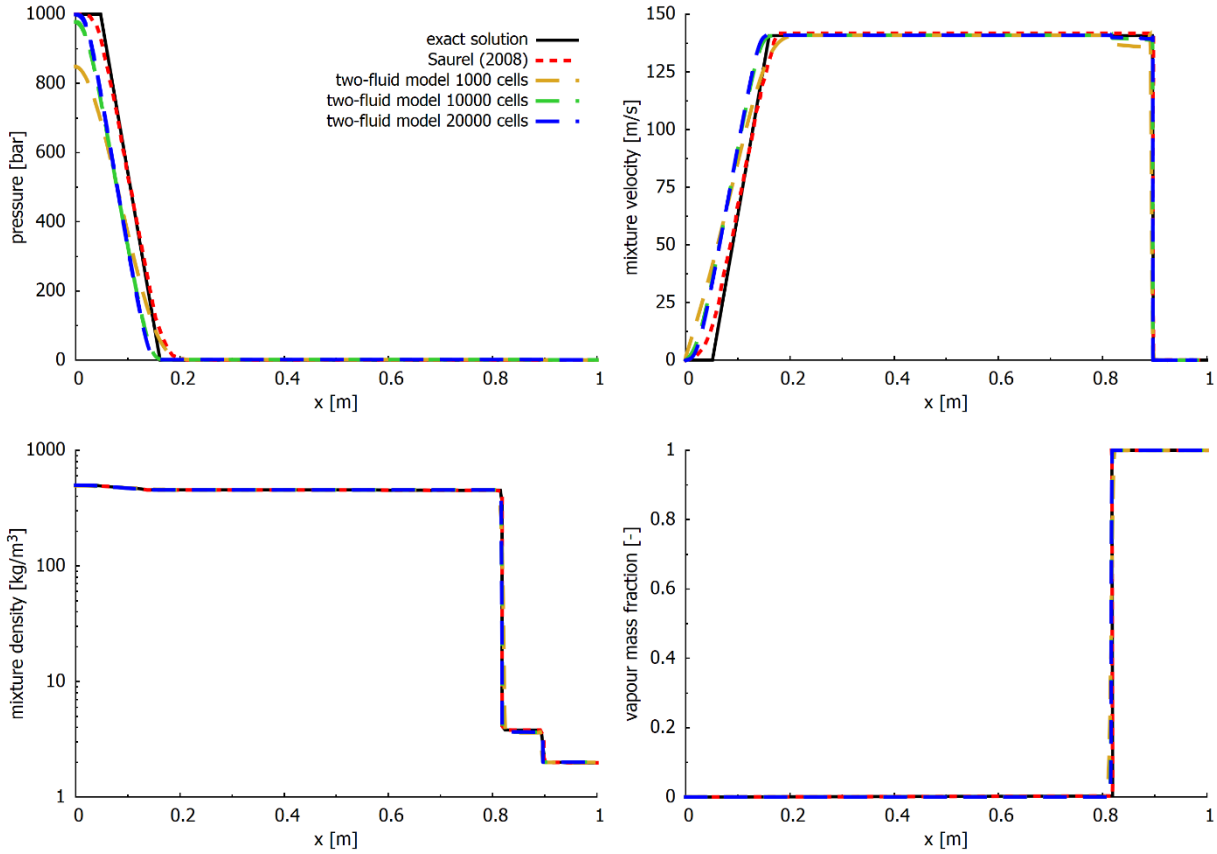

Figure 2 Dodecane liquid–vapour shock tube problem. Pressure, mixture velocity, mixture density and vapour dodecane mass fraction fields at 473μs after the initial contact discontinuity was removed. Comparisons between the exact solution and the numerical solutions of (Saurel, Petitpas and Abgrall, 2008) and the two-fluid model with different mesh resolutions.

3.2. Rising Bubble

The effective coupling between the two-fluid model and the implemented sharp interface method is evaluated against the behaviour of a rising bubble in a quiescent viscous liquid under the influence of the gravitational force. The dynamic deformation of a single rising bubble in a liquid column has been extensively examined with experimental studies (see selectively (Clift, Grace and Weber, 2005), (Bhaga and Weber, 1981), (Tomiyama *et al.*, 2002) among many others). Thus, the obtained bubble shape diagram, also known as the Grace diagram (Clift, Grace and Weber, 2005), depicts comprehensively a regime classification based on the final bubble shape and its terminal velocity as a function of dimensionless numbers. From a numerical perspective, a rising bubble simulation is commonly used to validate interfacial flow solvers, due to the high variety of interface deformation patterns under slightly modified flow conditions. For this purpose, in the absence of any analytical solution, (Hysing *et al.*, 2009) performed a two-dimensional numerical benchmark configuration with different codes and established a reference solution for two numerical cases of different density and viscosity ratios between the gas bubble and the surrounding liquid. A numerical benchmark case of an initially circular gas bubble rising in an initially stagnant liquid with liquid density 1000kg/m^3, liquid dynamic viscosity 10Pas and both density and viscosity ratios equal to 10, as proposed by (Hysing *et al.*, 2009) is used here for validation of the developed method. The gravity in the system is g=-0.98m/s^2 and the surface tension between the two fluids is σ=24.5N/m. Under these conditions, which correspond to intermediate Reynolds and Eotvos numbers with values 35 and 10, respectively, a moderate shape deformation is expected with a final bubble unbroken ellipsoidal shape based on the Grace diagram (Clift, Grace and Weber, 2005). The two-dimensional simulation was conducted with

the initial configuration and boundary conditions of Figure 3 in a uniform computational mesh of 320×640 cells.

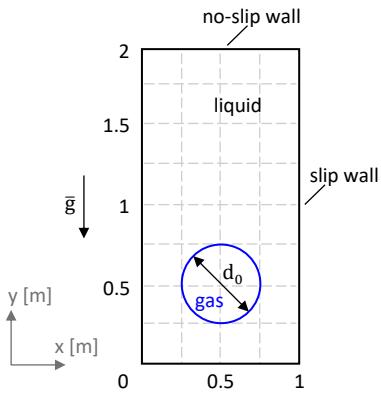

Figure 3 Initial configuration and boundary conditions for a two-dimensional circular gas bubble rising in a liquid column.

The rising bubble shape is presented in Figure 4 in three successive time instances and under the effect of different relaxation factor τ_r values, which appears in the artificial drag force of equation (8) as a case-dependent parameter to regulate an efficient coupling between the two-fluid model and the sharp interface approach. Focusing on the macroscopic evolution of the two-dimensional bubble interface, it is observed that the circular bubble is gradually deformed to an ellipsoid shape, due to the counter-action of gravitational and surface tension forces. Under the occurring ellipsoid regime (Clift, Grace and Weber, 2005), surface tension is dominant and mainly responsible for the evolution of a moderate bubble deformation without breakup of the interface. As it is also depicted in Figure 4, a stronger coupling between the two-fluid model and the sharp interface approach is achieved by maximizing the relaxation factor, corresponding to the elimination of the interfacial relative velocity. This numerical trick practically overcomes the two-fluid principle of the mathematical model, which imposes different velocity fields for each phase and approaches a standard sharp interface formulation, in which the two phases share a single momentum equation and respect the no-slip condition on the interface. Additionally, an increase of the relaxation factor, apart from the gradual elimination of the gas liquid relative velocity on the interface, has an apparent effect on the macroscopic bubble shape development.

However, the case-dependent calibration of τ_r has been avoided with the implementation of an on-the-fly algorithm which evaluates the interfacial region and gradually increases the value of τ_r, until the point that the tangential component of the relative velocity on the interface reaches a defined lower-bound close to zero. More specifically, in each iteration of the pressure correction the computational cells in the interfacial regions are evaluated to meet the no-slip condition. The criterion used relates the tangential component of the relative velocity on the interface with its total local value and sets a sufficiently low lower-bound, as follows:

$$\left|u_{r,tangential}\right| < 10^{-5}|u_r|$$

In the case that the above condition is not satisfied, the τ_r value is increased starting from the value of 1 for each interfacial cell in each new time step of the pressure correction algorithm. In order to avoid significant jumps on the drag force values and to improve the performance with reduction of the computation cost, a smoothing of the τ_r values in the neighbour cells is performed. A demonstration of the algorithm with different local values for τ_r with respect to the no-slip interface condition is illustrated in Figure 5 for the rising bubble. The maximum values for τ_r are observed on the sides of

the rising bubble, where also peaks in the relative velocity are observed due to the vertical motion of the bubble in the surrounding liquid.

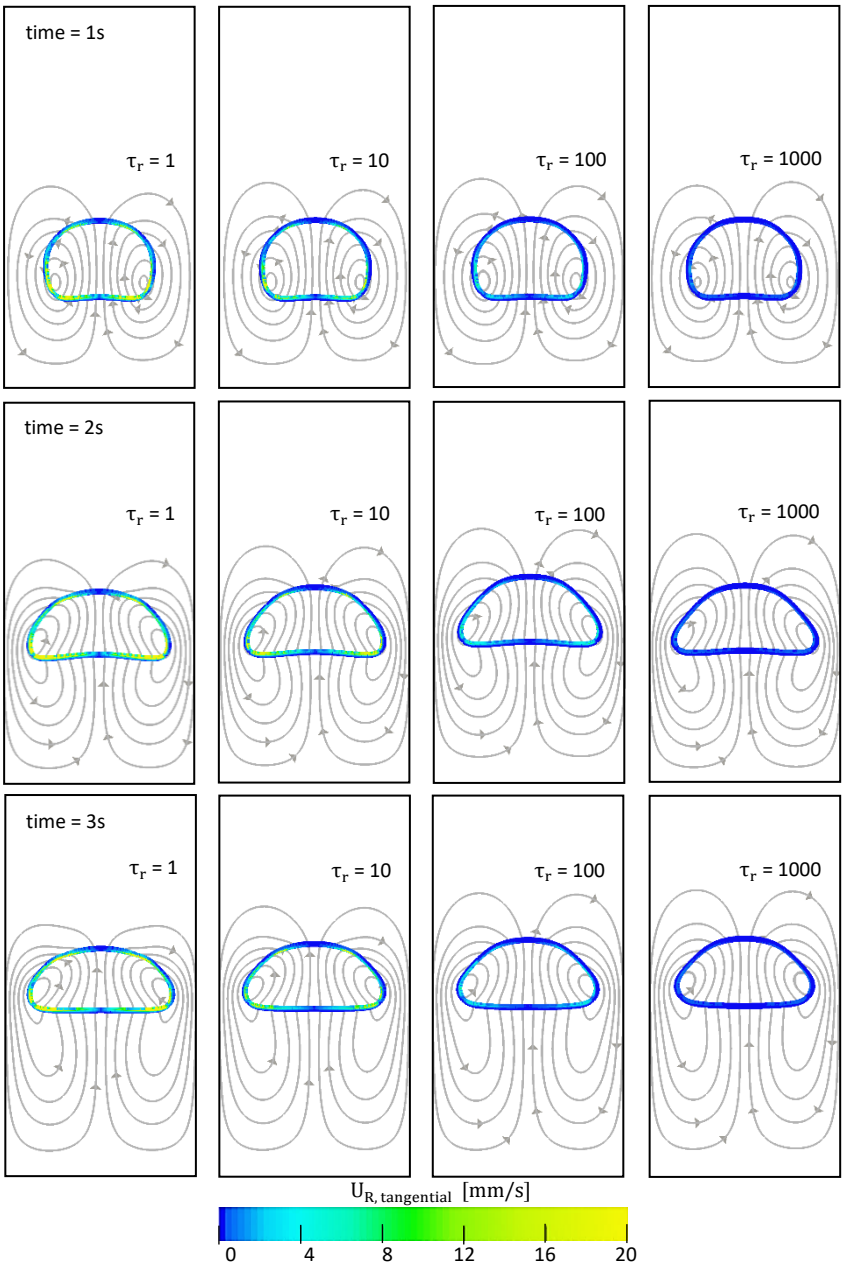

Figure 4 Tangential relative velocity distribution on the interface of a rising bubble and gas liquid mixture velocity vectors at successive times under the effect of different relaxation factors τ_r.

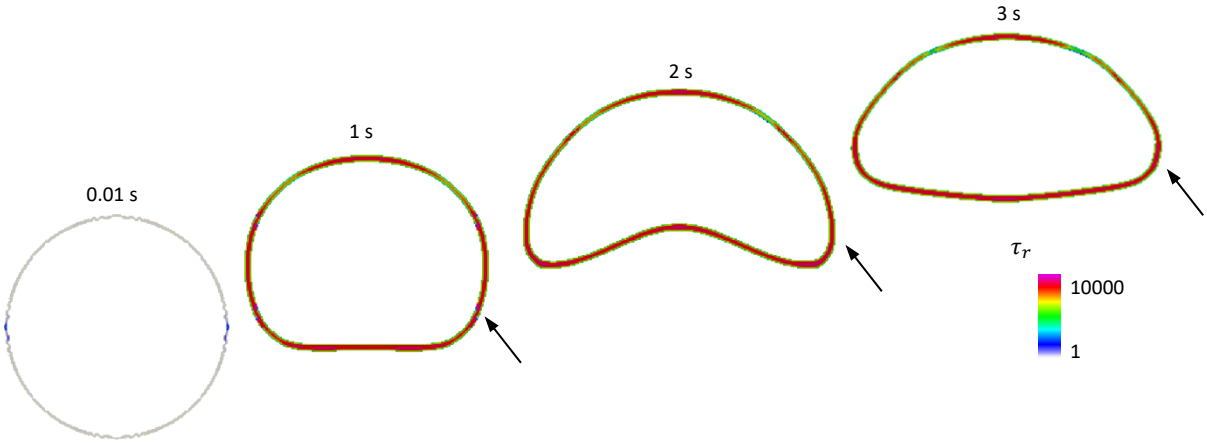

Figure 5 Relaxation factors τ_r calculated on the interface of the rising bubble with the on-the-fly algorithm for meeting the no-slip interfacial condition.

In the scope of a rigorous quantitative analysis, the mass centre position, the mean rise velocity and the deformed bubble circularity obtained with different relaxation factor values are examined in Figure 6. The computed benchmark quantities are compared with the reference solution of (Hysing *et al.*, 2009) and the results presented by (Štrubelj, Tiselj and Mavko, 2009), using a similar concept of coupling the two-fluid model with an interface sharpening approach; in this case, a conservative level set method has been utilised. Hereby, it is verified that a stronger coupling with the implementation of maximum value for the relaxation factor ensures that the evolution of the rising bubble will reach the expected behaviour. Specifically, the final position of the bubble centre of mass with the optimum relaxation factor τ_r=1000 is at 1.055m and differs 1.22% from (Štrubelj, Tiselj and Mavko, 2009) results. Furthermore, the maximum rise velocity is observed at 0.92s and with a value of 0.239m/s deviates by 2.58% from (Štrubelj, Tiselj and Mavko, 2009) solution. Regarding the bubble shape deformation, the minimum circularity value occurs at 1.98s, approximately 0.1s later than in (Štrubelj, Tiselj and Mavko, 2009) study; however, with respect to the tendency of circularity evolution in time the quantitative error is 1.7%. Finally, the shape of the rising bubble at its final position at 3s, as calculated with both the minimum and maximum relaxation factor values, shows the significant effect of an effective coupling between the two-fluid model and the sharpened interface approach on the bubble shape development with regards to the results in the literature (Hysing *et al.*, 2009), (Štrubelj, Tiselj and Mavko, 2009). The results obtained from the on-the-fly algorithm also meet a satisfactory agreement with the reference solution and show that the use of the proposed automatic algorithm for calibrating on-the-fly the relaxation factor τ_r is a good compromise to avoid any arbitrary case-dependent calibration and the significantly increased computational cost, when the artificial drag force is maximised in the whole interfacial region with an effect on the converge of the pressure correction algorithm.

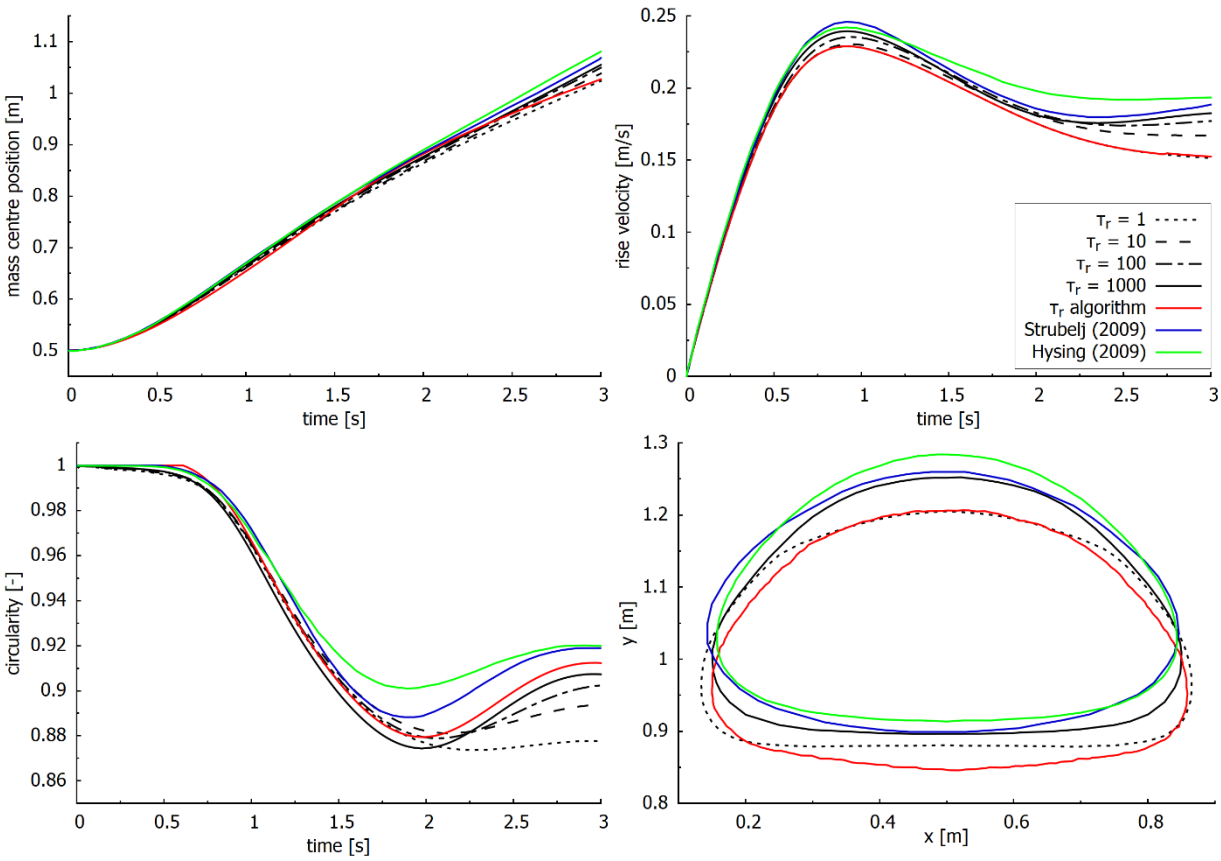

Figure 6 Bubble benchmark quantities, i.e. mass centre position, rise velocity and circularity, evolution in time under the effect of different relaxation factors τ_r. Bubble shape at its final position at 3s computed with minimum and maximum τ_r values. Comparisons with the reference solution of (Hysing *et al.*, 2009) and the simulation results performed by (Štrubelj, Tiselj and Mavko, 2009).

3.3. High-Speed Droplet Impact

3.3.1. Experimental Set-up

In order to validate the multiscale approach developed, new experiments have been performed for a droplet impact onto a solid surface. The experiments have been conducted at the University of Magdeburg and concern a water droplet impact onto a high-speed moving target in three different cases summarized in Table 2. The deionized water droplet is slightly deformed to an ellipsoid shape, due to the acoustic field which keeps it levitated; the droplet is hit by the flat and smooth moving target, propelled from an initial distance of 2.35m away from the levitating droplet. The experiments were performed at room temperature 21°C and atmospheric pressure conditions; the surface tension between the water droplet and the surrounding air is equal to 0.072N/m. The high-speed impact velocities of 120, 150 and 200m/s correspond to significantly high Weber and Reynolds numbers both of the order of 10^5 to 10^6, as calculated for the droplet properties at impact conditions. The rapid droplet splashing and the subsequent violent fragmentation of the produced secondary structures were visualized with the use of a high speed camera of 5 million frames per second and a spatial resolution of 50µm per pixel; recording of video started when the moving target was approximately 3.17mm away from the droplet.

Table 2 Impact conditions for the examined experimental cases of high-speed droplet impact on a moving target.

case	d_x [mm]	d_y [mm]	u_{imp} [m/s]	target	We [-]	Re [-]	Oh [-]
1	2.017	1.55	120	teflon	3.6×10^5	2.2×10^5	7.6×10^{-3}
2	2.65	2.2	150	teflon	7.6×10^5	3.7×10^5	5.5×10^{-3}
3	2.14	1.796	200	acrylic	1.1×10^6	4.2×10^6	6.9×10^{-3}

3.3.2. Simulation Results

For the numerical simulations of high-speed droplet fragmentation, the problem is set-up in a different but corresponding manner with the water droplet moving with the impact velocity towards a rigid wall target. The simulations were performed in a 3D wedge geometry with one cell thickness, using a computational mesh of 412,500 cells; the details are described in Figure 7. For the purpose of a grid dependency investigation regarding the multiscale model functionality, two additional computational meshes have been used with twice coarser and twice finer resolution compared to the original mesh in the region around the droplet and wall interaction, illustrated as zone I in Figure 7. At the initial time step the moving droplet is set 0.9mm away from the rigid wall. Apart from the liquid phase velocity field, which is initialized with the initial velocity of the moving droplet, the air velocity field is also initialized from a developed field obtained with the impact velocity set as an inlet in the right patch of the computational domain. Using this configuration, the effect of the moving target on the surrounding air in the original experimental set-up is adequately represented in the conducted simulations. The liquid gas interface surface area density is initialized on the droplet interface as the surface area of an ellipsoid with the dimensions of the examined water droplet which corresponds to a 5° wedge per unit of the local computational cell volume. On the wall, the no-slip boundary condition is applied for the velocity fields, while a Neumann boundary condition is satisfied for the other computed flow fields.

The spatial discretization used is based on second order linear discretization schemes, limited towards a bounded first order upwind scheme in regions of rapidly changing gradients. Time stepping is performed adaptively during the simulation, so as to respect the selected limit for the convective Courant–Friedrichs–Lewy (CFL) condition of 0.4. Even though the turbulent state corresponds to fully 3D-developed phenomena, the evolution of the droplet fragmentation under the examined impact conditions is found to be significantly quicker compared to the turbulence time scales. Therefore, the configuration of Figure 7, which is utilised in the performed simulations, is an acceptable compromise between the accuracy of the numerical model and a viable computational cost.

The simulations conducted were based on the assumption that the liquid phase is the only present dispersed phase, interpenetrating and interacting with the continuous air phase. Under the high-speed impact conditions corresponding to very high Weber numbers ranging from 10^5 to 10^6, the droplet impact on the wall and the imposed prompt splashing will evolve rapidly; thus, contact angle boundary conditions are not explicitly defined and a zero gradient boundary condition for the water volume fraction on the wall is imposed (Kyriazis, Koukouvinis and Gavaises, 2018). With regards to phase-change phenomena, vaporisation plays a minor role at the early stages of impact, since the temperature variations around the room conditions are not significant in comparison to the other physical phenomena that take place (Kyriazis, Koukouvinis and Gavaises, 2018). Specifically, in the present simulations the local water temperature does not increase more than 20K at the moment of impact, when the strong shock wave is formed inside the droplet and the maximum local pressure of about 10^8Pa is observed. On the contrary, cavitation is produced inside the droplet due to the influence of strong compressibility effects; however, in this particular case its influence is negligible

compared to other dominant physical phenomena and it is not taken into consideration in the numerical modelling, as it is analysed in detail in the following paragraphs.

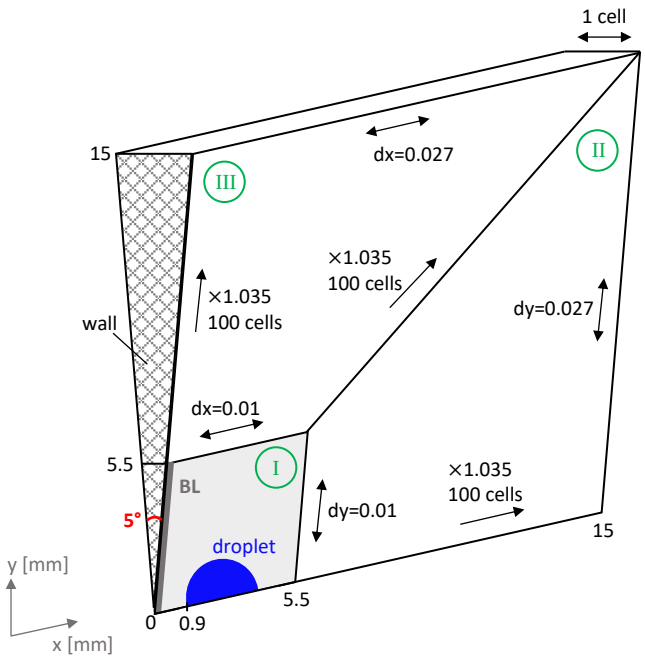

Figure 7 Initial configuration and information regarding the computational mesh for the simulation of high-speed droplet impact on a rigid wall.

The evolution of the droplet fragmentation at 2, 4 and 6μs after the impact on the target are presented in Figures 8, 9 and 10, respectively, as it has been captured by the experimental study and the performed simulations with the proposed multiscale two-fluid model under the three different impact conditions of Table 2. In the numerical investigation, the widespread and highly dispersed water cloud produced after the prompt splashing of the droplet is subject to the diffuse interface formulation of the multiscale two-fluid model, shown as a grey iso-surface in the results. Therefore, the dominant sub-grid scale structures are modelled accordingly within the dispersed flow regime formulation of the numerical model and the interface surface area density diameters are calculated and used in the drag force calculations. Despite the vast spectrum of scales involved, the macroscopic characteristics of the successive stages of the droplet fragmentation are adequately predicted by the performed simulations, with the corresponding results to depict the radially expanding water cloud. In cases 1 and 2, which correspond to Weber numbers at impact conditions of the order of 10^5, a similar evolution of the phenomenon is observed with an expected more rapid water dispersion under the impact velocity of 150m/s. On the contrary, in case 3 the increase in the Weber number of the order of 10^6 results to a significantly violent droplet splashing with a widespread water cloud corona to be captured both by the experimental results and the simulation. However, the water microjet injected from the centre of the deforming droplet surface opposite to the droplet motion, which is depicted in the experimental captures as an effect of the secondary cavitation formation inside the droplet, is a low intensity phenomenon compared to the dominant and rapid water dispersion.

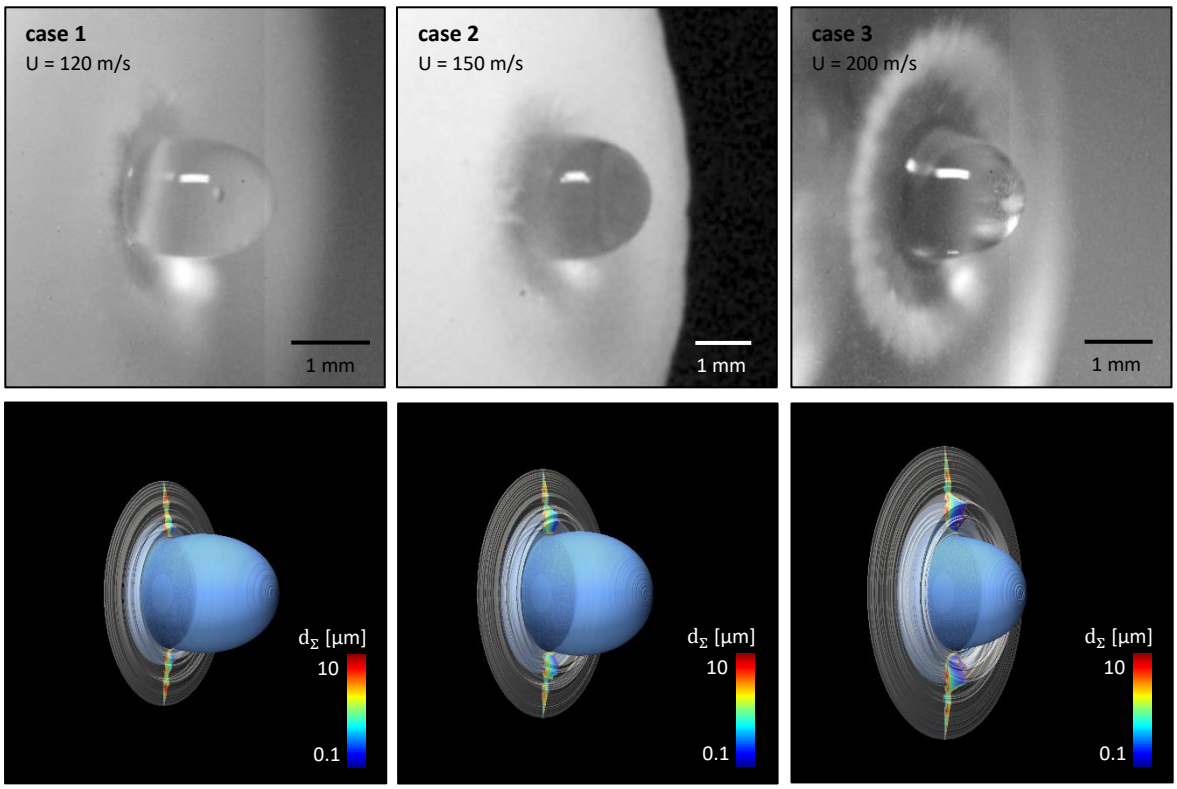

Figure 8 Droplet fragmentation 2μs after impact on the target in cases 1, 2, 3. Comparison between the experimental results captured 32° from the perpendicular view and the 3D reconstructed flow fields from the simulation. Blue iso-surface represents the sharp interface regions and grey iso-surface the diffuse interface regions calculated with the multiscale two-fluid approach.

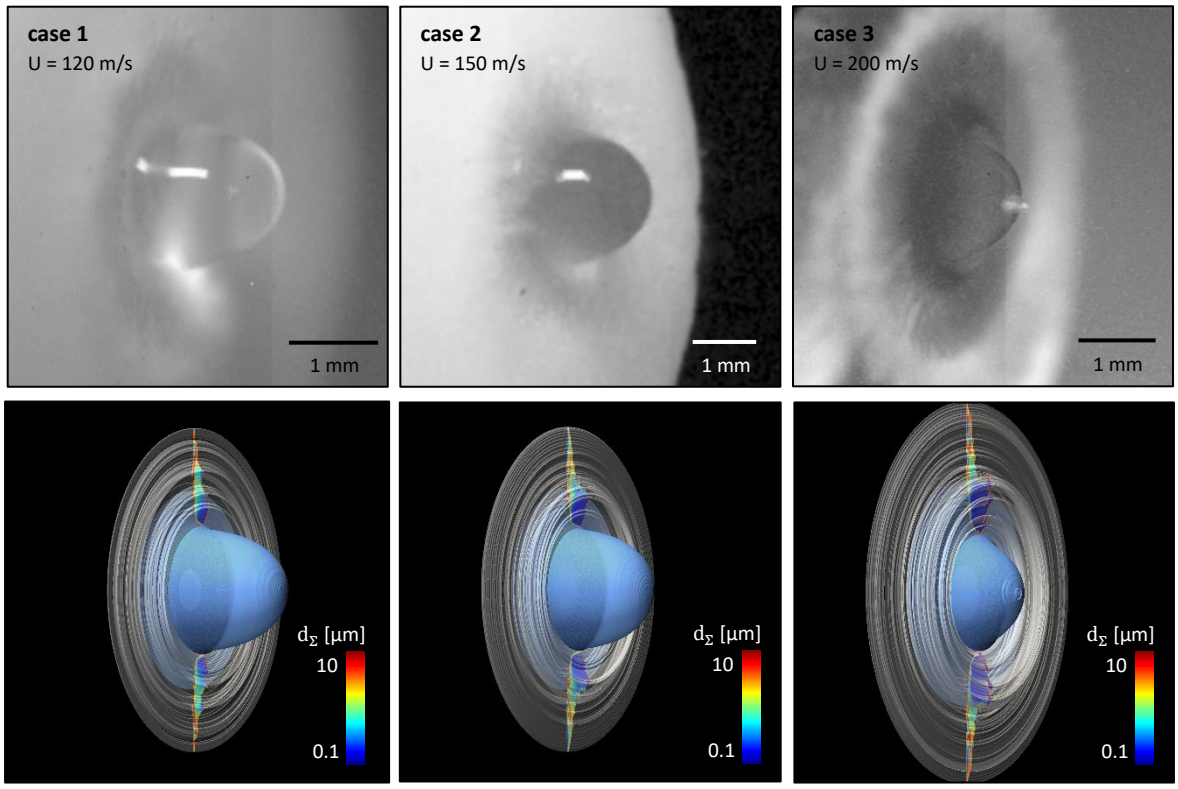

Figure 9 Droplet fragmentation 4μs after impact on the target in cases 1, 2, 3. Comparison between the experimental results captured 32° from the perpendicular view and the 3D reconstructed flow fields from the simulation. Blue iso-surface

represents the sharp interface regions and grey iso-surface the diffuse interface regions calculated with the multiscale two-fluid approach.

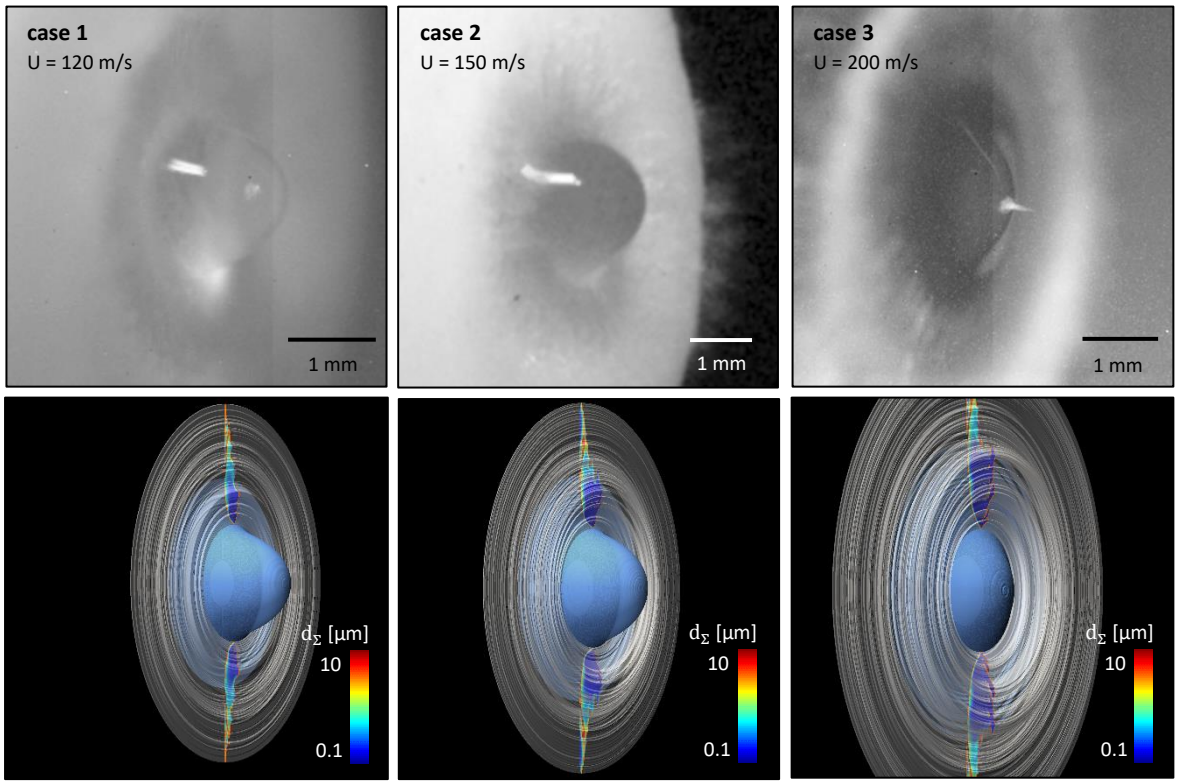

Figure 10 Droplet fragmentation 6μs after impact on the target in cases 1, 2, 3. Comparison between the experimental results captured 32° from the perpendicular view and the 3D reconstructed flow fields from the simulation. Blue iso-surface represents the sharp interface regions and grey iso-surface the diffuse interface regions calculated with the multiscale two-fluid approach.

The evolution of the droplet impact with the target under the impact velocity of 150m/s (case 2), the prompt splashing at the early stages of impact along with the severe fragmentation and water dispersion at later stages are presented in Figures 11 and 12. In successive time instances, the experimental video snapshots are compared with the 3D reconstructed water volume fraction iso-surface at 10^{-3} obtained from the performed simulations with the proposed multiscale two-fluid model and the compressibleInterFoam solver, which is based on a VOF method commonly used for this type of problems. The iso-line of the water volume fraction at a value of 10^{-5}, as calculated with the multiscale two-fluid approach, is plotted against the experimental results. Moreover, the detected dispersed flow regions using 3 different computational grids, namely the original grid of Figure 7 along with two new grids with twice coarser and twice finer resolution in region I, respectively, are presented to depict the dependency of the interfacial approaches capabilities and the performed topological investigation on the local mesh resolution.

As it can be observed in Figure 11, at the moment of impact the flow field is dominated by a segregated flow regime with perfectly separated two phases as defined by the droplet interface. Thus, up to this point, the sharp interface approach is applied exclusively in the whole flow field; good results are obtained with respect to the initial droplet shape. At that time, the occurring impact conditions correspond to a very high Weber number of 7.6×10^5 and thus, a prompt splashing is imposed driven by the dominant droplet inertia. Subsequently, the violent impact conditions do not allow for a liquid lamella to be formed, as depicted in the experimental results; instead, the production of a dense cloud of secondary droplets and ligaments is observed, which is moving radially ahead of the deformed

droplet. At these stages, which correspond to times 1-3μs in Figure 11, the topological algorithm detects the first transitions in the dispersed flow regime; the cloud of the produced fluid structures after the droplet and wall impact is subject to a diffuse interface approach, since it consists of structures smaller than 10^{-5}m that cannot be resolved by the local mesh resolution. On the contrary, the simulation with the VOF method applied in the whole flow field captures accurately the tendency of a radial water expansion. However, the overall sharp interface formulation leads to the prediction of an unphysical thin water film after the impact, as in the case of a well-formed lamella under moderate impact conditions, instead of the experimentally observed wide cloud of secondary droplets. This predicted behaviour corresponds to the deficiency of the VOF method to resolve small fluid structures in the sub-grid scale limit. As a result, the computational cells with relatively small volume fractions, that imply the existence of microscale secondary droplets, are underestimated and therefore, a thin water film is calculated in the regions of a high water volume fraction concentration. It is interesting to notice that at the examined early stages of impact, the multiscale two-fluid model with a finer mesh can predict more accurately the extent of the water spatial dispersion compared to the original or an even coarser mesh, as it is illustrated in Figure 11 at 2 and 3μs. Given the fact that large-scale structures dominate the dispersed regions at the first time instances after impact, it is expected that a finer mesh can obtain most of the flow field information with the multiscale model to operate under a diffuse interface approach. Nevertheless, this is not the case for the later stages of impact, in which the microscale droplets overtake the larger initially produced droplets of the dense water cloud, as it will be discussed afterwards.

Later stages of the droplet impact are depicted in Figure 12, where the flow is highly dispersed with an extended cloud of secondary features expanding radially away from the target. A widespread dispersed region in the form of an expanding corona is also captured by the multiscale two-fluid model; however, the calculated radial water dispersion is limited compared to the experimental observation. More specifically, after 4μs in regions of apparent water concentration in the experiment, approximately 1 mm away from the target, there is not any significant amount of water volume fraction present in the simulation. Moreover, as shown in Figures 8, 9, 10, the smaller structures are underestimated at the outer sides of the expanding cloud and the mixing of the injected water with the surrounding air is limited. Due to the supersonic conditions of the expelled surrounding air at the later stages of impact and the significant increase in local air temperature, vaporisation may be the key mechanism of water dispersion at the borders of the expanding water cloud; thus, the consideration of vaporisation effects should lead to an improved and more realistic capturing of the extended water dispersion at the later stages of impact. However, as it is comprehensively presented in Figure 13, the vertical expansion of both the attached on wall water film and the dispersed secondary droplets cloud is well predicted with the performed simulation under the existing highly multiscale conditions in the course of the impact and meets satisfactorily the experimental measurements for the lower values of the water volume fraction. Therefore, the obtained results provide a relatively accurate insight into the presence of an extended and chaotic water dispersion in contrast to the VOF method results, which are restricted to a non-realistic water film spreading with only a few droplets being formed as a numerical result of the strict sharp interface implementation. Within the scope of a grid dependency analysis, it is noticeable in Figure 12 that for the occurring dominant dispersed flow regime, a coarser computational mesh along with the multiscale approach can provide locally a more extended radial water dispersion region. Some of the original computational cells with negligible water volume fraction are now incorporated to neighbour cells and therefore, are subject to a diffuse interface regime for the modelling of local sub-grid scale secondary droplets with dimensions even less than 1μm. This behaviour comes in contrast to the results obtained with the multiscale approach and a finer mesh, which predict a limited radial water

spreading and approach the results of the pure VOF simulation. Consequently, the application of the multiscale two-fluid model in flow regions with multiple dynamic transitions between the segregated and dispersed regimes using a locally uniform computational grid, as performed in the conducted simulations, requires a compromise regarding the selected grid resolution. More specifically, given the numerical limitations of the VOF and the diffuse interface methods with respect to the computational grid and the switching criteria of the flow topology detection algorithm, an intermediate grid resolution is defined as optimum.

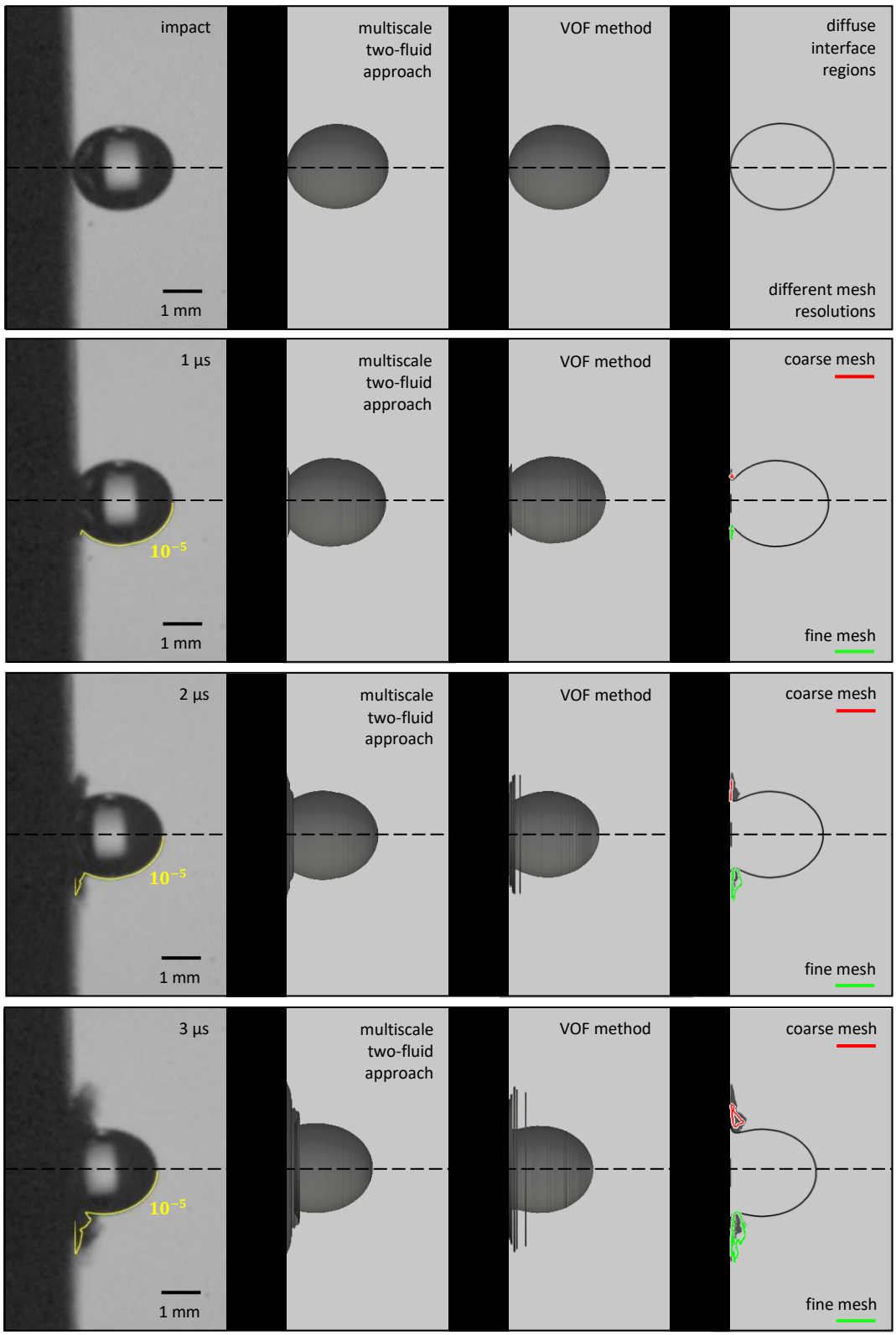

Figure 11 Early stages of droplet impact with the target under the impact velocity of 150m/s (case 2). Comparisons between the experimental results from side view and the 3D reconstructed water volume fraction iso-surface at 10^{-3} obtained with the multiscale two-fluid model and the VOF method. The diffuse interface regions, calculated with the multiscale two-fluid model using 3 different mesh resolutions, are compared in the last column. Yellow iso-line represents the water volume fraction at 10^{-5}, red isoline the diffuse interface regions using a coarse mesh and green isoline the diffuse interface region using a fine mesh.

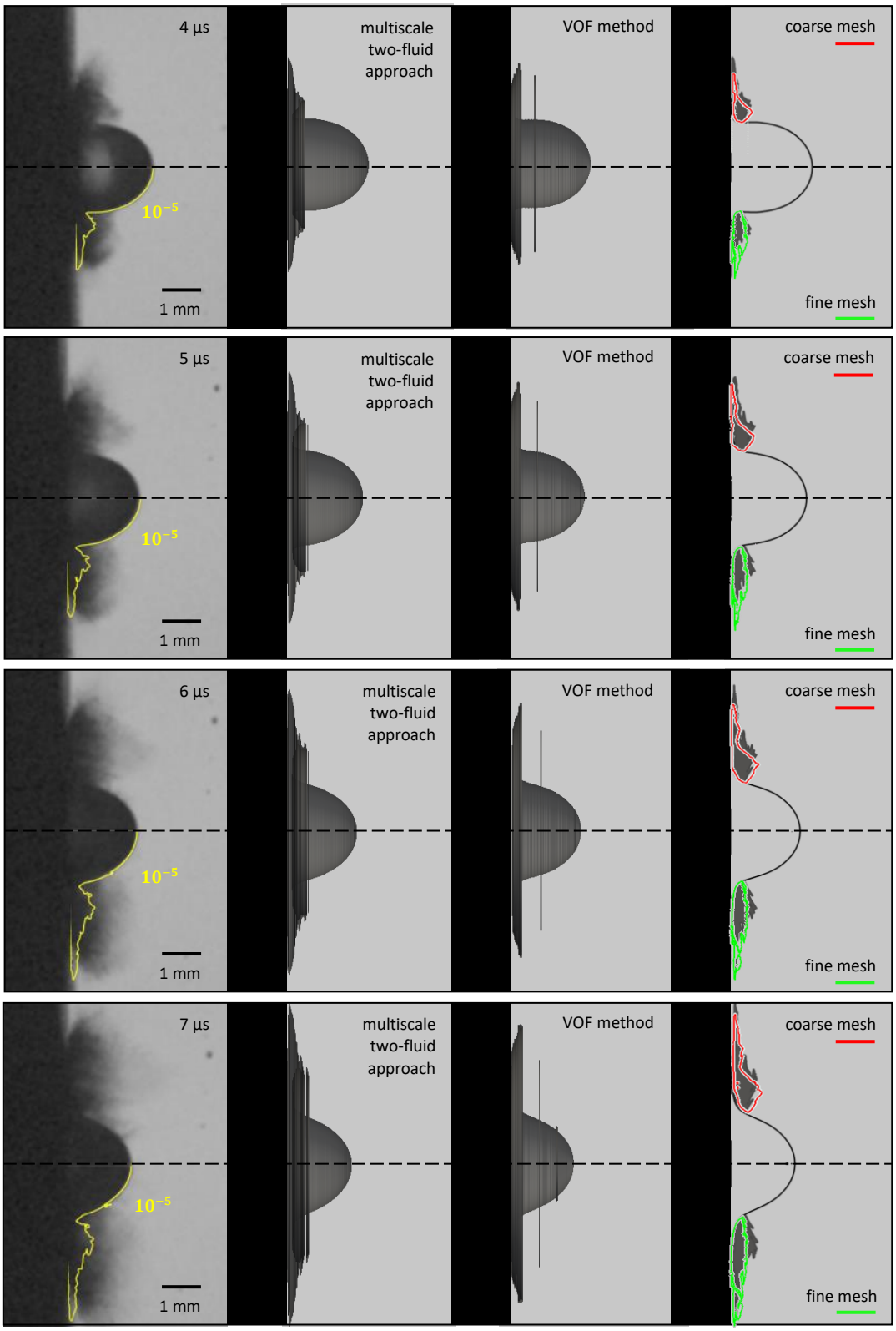

Figure 12 Later stages of droplet impact with the target and intense water dispersion under the impact velocity of 150m/s (case 2). Comparisons between the experimental results from side view and the 3D reconstructed water volume fraction iso-surface at 10^{-3} obtained with the multiscale two-fluid model and the VOF method. The diffuse interface regions, calculated with the multiscale two-fluid model using 3 different mesh resolutions, are compared in the last column. Yellow iso-line represents the water volume fraction at 10^{-5}, red isoline the diffuse interface regions using a coarse mesh and green isoline the diffuse interface region using a fine mesh.

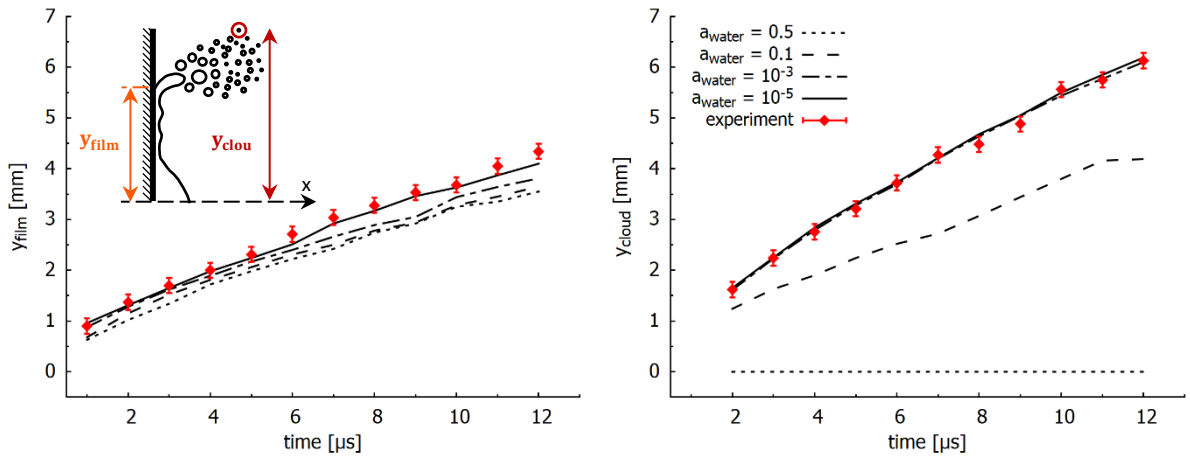

Figure 13 Droplet fragmentation under the impact velocity of 150m/s (case 2). Comparisons between the experimental and the numerical results with different water volume fraction values for the vertical expansion of the attached on wall water film and the secondary droplets cloud.

The high-speed droplet impact is governed by significant compressibility effects inside the droplet at the early stages of the interaction with the rigid wall. After the moment that the droplet reaches the wall, a strong shock wave is formed inside the droplet with local pressure up to 1200bar, as depicted in Figure 14 at 0.4μs. The shock wave is propagating and moving outwards, opposite to the droplet motion, while it gradually overtakes the contact line between the target and the deforming droplet. At 1.7μs it is observed that the shock wave is reflected normal to the droplet outer free surface and an expansion wave adjacent to the free surface is created (Haller *et al.*, 2002), (Wu, Xiang and Wang, 2018). Afterwards, the shock wave propagation continues with the formation of an increasing low pressure region inside the droplet, until the time it reaches the boundary of the deforming droplet interface and it is reflected backwards at 2.7μs. This shock wave reflection results to the creation of strong rarefaction waves (Haller *et al.*, 2002), (Wu, Xiang and Wang, 2018) at 2.9μs, which could result to extended cavitation regions inside the droplet. However, it has been shown in previous numerical studies (Niu and Wang, 2016), (Kyriazis, Koukouvinis and Gavaises, 2018), (Wu, Xiang and Wang, 2018) that under similar conditions the produced vapour volume fraction after the shock wave reflection does not exceed the value of 0.03, defining a non-significant cavitation effect. Since the droplet impact evolution is not driven by cavitation under the examined impact conditions, a model for cavitation has not been implemented in the developed multiscale framework; instead, a very small volume fraction of air of order of 10^{-6}, which corresponds to the nucleation volume fraction, is introduced in the initial droplet volume fraction. Under this assumption, the small gaseous volumes inside the droplet will expand after the significant pressure drop, leading to volumes equal to those that would occur with cavitation. The pressure evolution inside the droplet will continue with the gradual elimination of the created regions of small gaseous volumes, as long as the droplet widespread splashing is dominating the surrounding flow field.

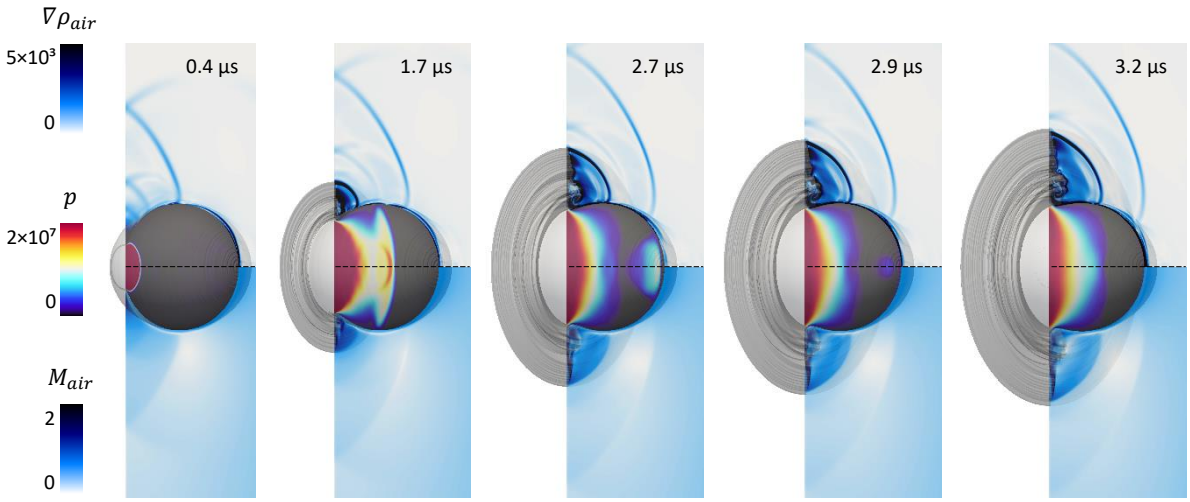

Figure 14 Time evolution of the pressure field inside the droplet, the shock wave formation and propagation along with the density gradient and the Mach number for the surrounding air after the droplet impacting the rigid target with a velocity of 150m/s (case 2).

After the droplet impact and along with the beginning of a strong shock wave propagation inside the droplet, the development of a high speed jetting is observed in Figure 15. The injected water film, which just after the droplet impact at 1μs has a velocity 5 times larger than the impact velocity, is responsible for the rapid lateral and radial water dispersion. This observation also meets the experimental measurements of a maximum liquid film expanding velocity at around 720m/s. At the same time, a supersonic flow with strong propagating shock waves is observed in the surrounding air, due to the high speed dispersion of the produced water cloud. As illustrated in Figure 14, the formation and high-speed injection of the water film at the early stages of the droplet impact, corresponds to a violent displacement of the surrounding air, resulting to a supersonic flow for the air with local Mach numbers up to 2.5. Subsequently, during the droplet lateral spreading on the wall target, the intensity of the initial jetting and the propagating shock waves in the air is reduced; however, the velocities of the water phase remain significant with peaks on the dispersed flow regions where the secondary droplets cloud is penetrating the surrounding air. An examination of the temporal and spatial evolution of the relative velocities between the droplet and the surrounding air in Figure 15 comes to the same conclusion that the highest water velocities occur at the borders of the expanding water cloud. Thus, in highly dispersed flow regions, where practically very small droplets are present, the consideration of aerodynamic and slip velocity effects increases the physical coherency of the numerical model.

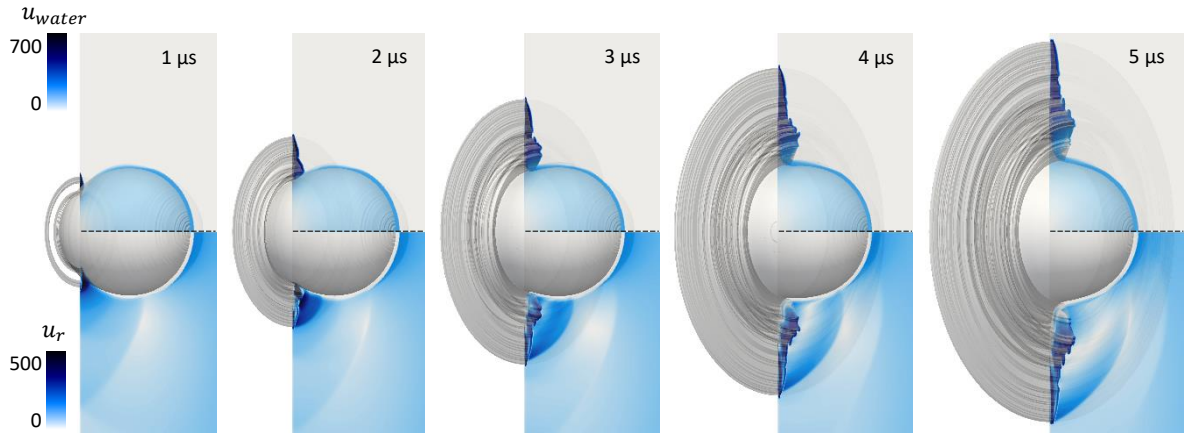

Figure 15 Time evolution of the water velocity field inside the droplet and the relative velocity field in the surrounding area after the droplet impacting the rigid target with a velocity of 150m/s (case 2).

In Figure 16 the temporal evolution of the calculated interface surface area under different impact velocities is presented, as it is obtained from the transport equation for the liquid gas interface surface area density (5). A similar pattern regarding the interface surface area production over time is observed irrespectively of the impact conditions. More specifically, after the droplet impact the interface surface area is gradually increasing with the same rate till approximately point A. These time instances, as shown in Figure 17, correspond to the early stages of splashing, where the water film lateral spreading on the wall target dominates the formation and expansion of the dispersed water cloud. Since the surface area of the undeformed droplet interface remains unchanged, the maximum values of the interface surface area are observed on the dispersed regions away from the wall target where sub-grid scale turbulent mixing and secondary droplet coalescence and breakup have a crucial effect on interface production, as described in equation (5). After that and until approximately point B in Figure 16, the interface surface area performs a rapid increase which is more intense with an increase on the impact velocity and is related to later stages of the fragmentation evolution with the water dispersion becoming the main effect on interface production. After point B and until the end of the observation of the phenomenon, an almost smooth increase in interface surface area is shown due to the penetration of the already produced secondary droplets cloud in the surrounding area.

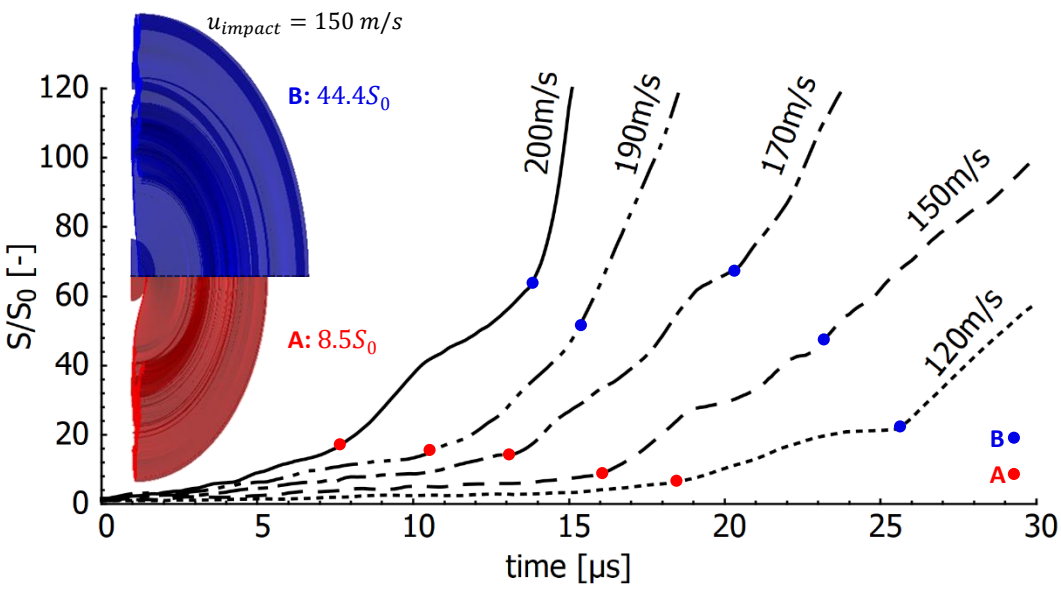

Figure 16 Time evolution of the interface surface area for the developed water cloud and the secondary flow features after the droplet impact on wall with respect to the initial ellipsoid droplet surface area S_0 under different impact velocities. As time zero is set the moment of impact onto the rigid wall for the droplet with impact velocity 150m/s.

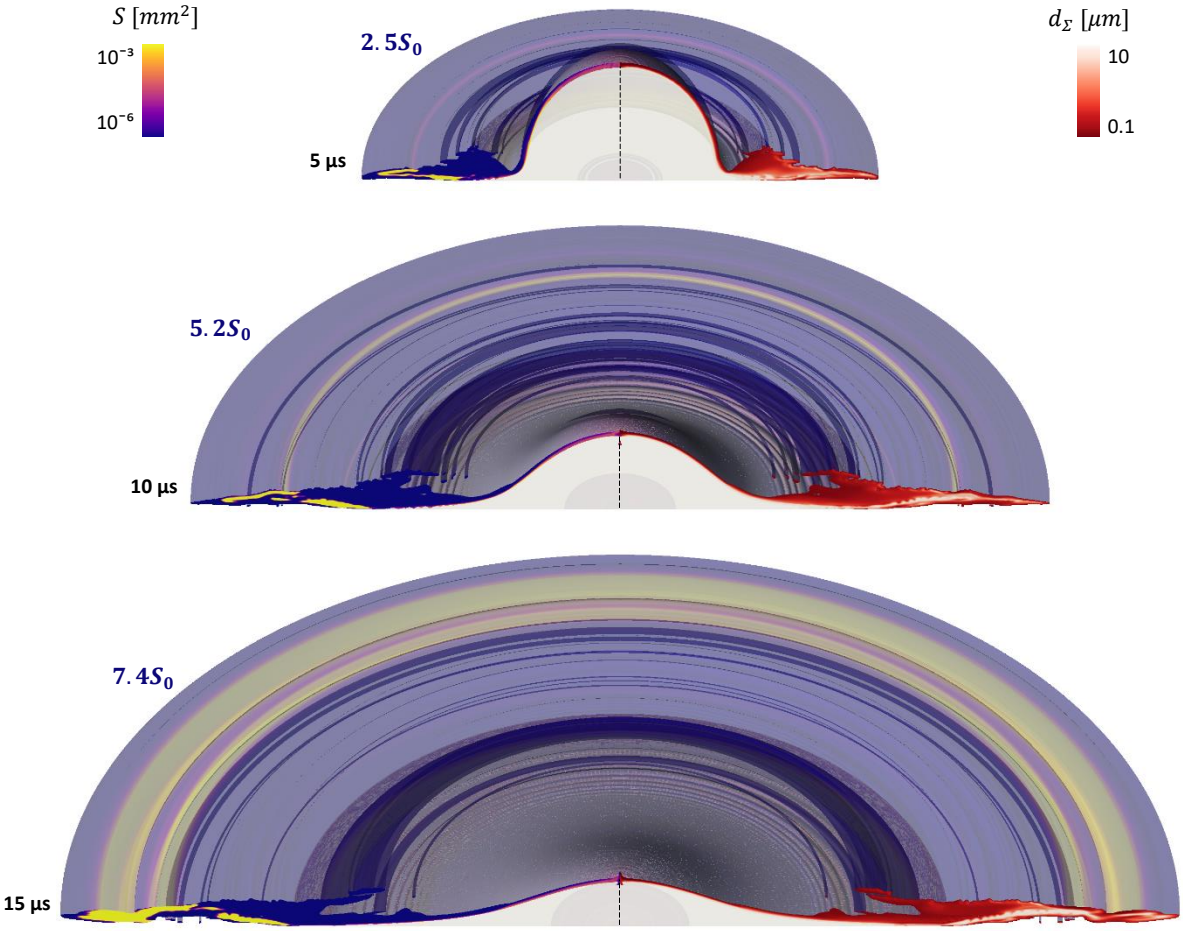

Figure 17 Characteristic instances of the interface surface area evolution with respect to the initial ellipsoid droplet surface area S_0 and the calculated interface surface area density diameters under the impact velocity of 150m/s (case 2).

In Figure 18, two characteristic time instances at the earlier and later stages of the droplet fragmentation under the impact velocity of 150m/s are selected to depict the functionality of the flow topology detection algorithm. On the left side of the axis of symmetry are illustrated the calculated diameters based on the interface curvature d_{curv}, which are used for the first geometric criterion of equation (16) in the sharp interface regions. As shown, the local interface curvature can obtain relatively large values which based on equation (15) are correlated with small fluid structures, reaching the limit of the local mesh resolution and the accuracy capabilities of the sharp interface approach. However, only the geometric criterion is not sufficient to keep a physical consistency regarding the areas of small d_{curv} values, with such small fluid structures to be detected even in areas inside the deforming droplet core where the presence of small droplets has no physical interpretation. Thus, the additional topological criteria are the key factor in introducing a switching between sharp and diffuse interface approaches with respect to the local flow development and the physical transition from a segregated to a dispersed flow regime. The computational cells which satisfy both the geometric and the topological criteria and are subject to a diffuse interface formulation in the following time step are marked in green. As expected, these regions are detected at the borders of the already diffuse interface regions within the dispersed water cloud and they concern relatively large flow structures, which were previously resolvable by the mesh resolution with local minimum cell sizes of 10^{-5}m. On the right side of figure 18 the calculated interface surface area density diameters d_{Σ} for the currently diffuse interface region within the highly dispersed secondary droplet cloud are illustrated. As shown, the local diameters used for the local drag force calculation range from the spectrum of microscales to 10^{-5}m, which is the local minimum cell size and correspondingly the limit for a sub-grid scale analysis. In both time instances there are detected a few computational cells in the borders between sharp and diffuse interface approach regions with d_{Σ} that exceed the local cell dimensions; these computational cells are subject to a sharp interface approach based on the geometric criterion of equation (17).

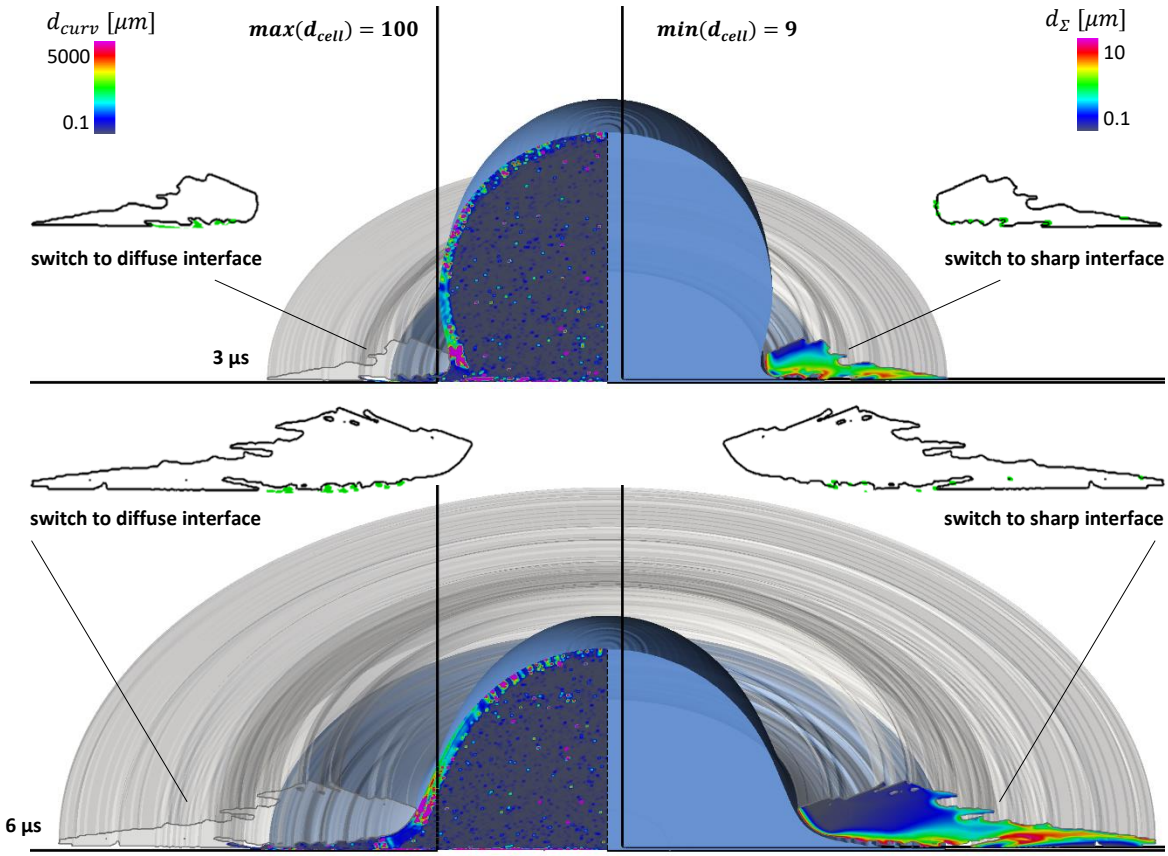

Figure 18 Droplet fragmentation with impact velocity 150m/s (case 2). Blue iso-surface represents the sharp interface regions and grey iso-surface the diffuse interface regions calculated with the multiscale two-fluid approach. (on the left) The calculated diameters based on the interface curvature. In green are marked the cells switching from sharp to diffuse interface approach. (on the right) The calculated interface surface area density diameters. In green are marked the cells switching from diffuse to sharp interface approach.

Considerable emphasis has been put on correlating the geometric switching criteria of the flow topology detection algorithm, which in essence act as an indication for the numerical capabilities of the sharp and diffuse interface approaches, with the physically observed transition between different flow regimes during the flow development. Therefore, in Figure 19 are presented the Weber and Reynolds numbers for the dispersed secondary droplets after impact, which are subject to an aerodynamic breakup induced by the relative velocity between the injected droplet with calculated diameter d_{Σ} and the expelled surrounding air. As illustrated for successive time instances, the flow development after impact is restricted by the limit of Ohnesorge numbers less than 0.1, which indicates that the produced secondary droplets breakup is mainly controlled by the droplet Weber number (Guildenbecher, Lopez-Rivera and Sojka, 2009). Additionally, only inside the diffuse interface region are observed Weber numbers with values larger than 0.5, which correspond to the beginning of the droplets oscillation and deformation (Guildenbecher, Lopez-Rivera and Sojka, 2009), confirming that the flow topology detection predicts accurately the dispersed flow region. Within the diffuse interface region and closer to the edges of the radially expanding cloud of secondary droplets are detected regions with increasing Weber number and values larger than 10, which is set as a limit for the droplet aerodynamic breakup (Guildenbecher, Lopez-Rivera and Sojka, 2009).

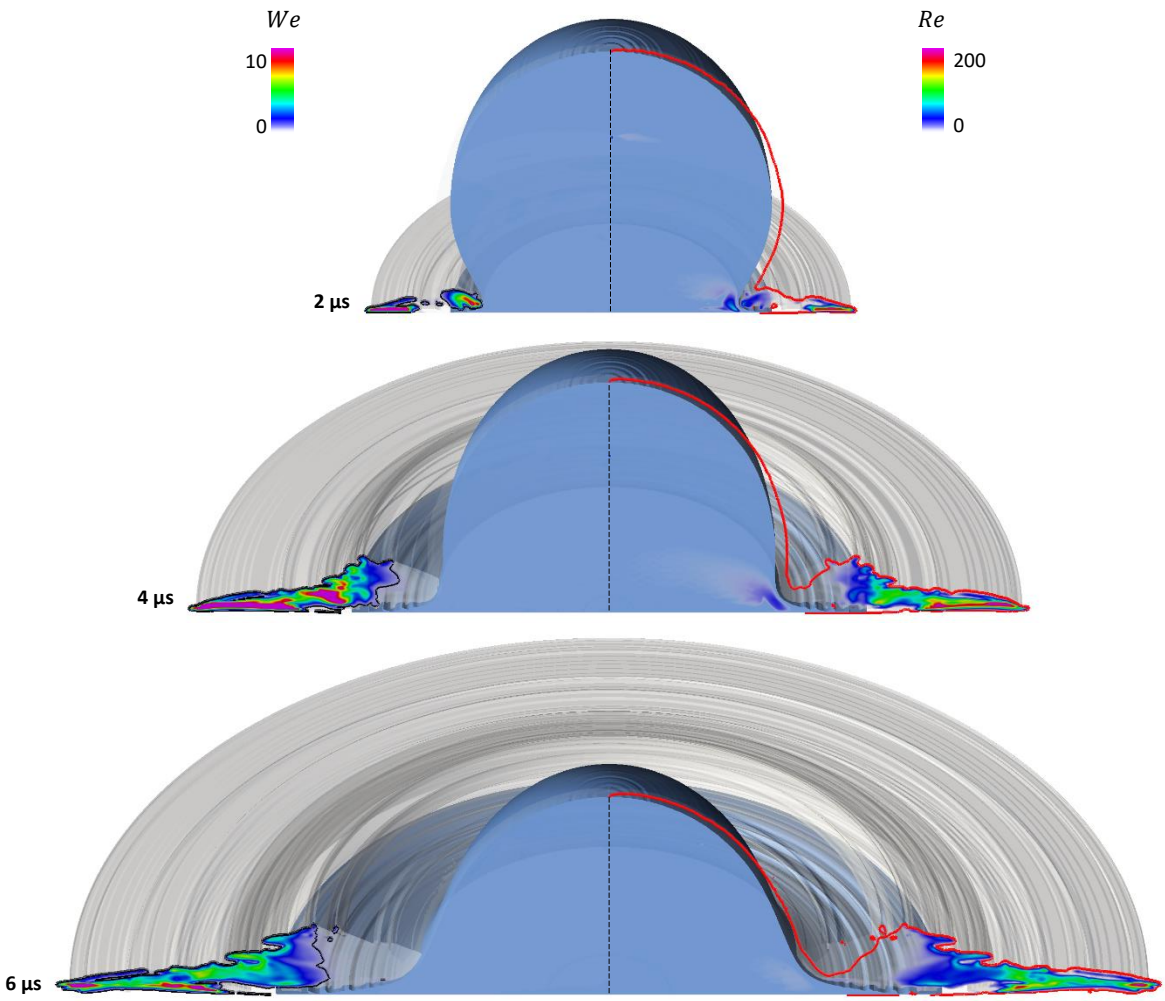

Figure 19 Droplet fragmentation with impact velocity 150m/s (case 2). Blue iso-surface represents the sharp interface regions and grey iso-surface the diffuse interface regions calculated with the multiscale two-fluid approach. (on the left) The Weber number field for the aerodynamic breakup of the produced secondary droplets after impact. Black iso-line corresponds to Weber number value of 0.5. (on the right) The Reynolds number field for the aerodynamic breakup of the produced secondary droplets after impact. Red iso-line corresponds to Ohnesorge number value of 0.1.

4. Conclusion

A compressible Σ-Y two-fluid model with dynamic interface sharpening based on local topological criteria has been developed and implemented in OpenFOAM ®. The aim of the present study was to simulate highly compressible flows with significant slip velocity effects and multiscale complexities using a uniform solver, which detects dynamically the different coexisting flow regimes and operates under the most appropriate formulation. The numerically challenging coupling of a two-fluid model with an interface sharpening method has been examined and validated against a benchmark case of a shock tube and a rising bubble, obtaining useful results on how eliminating the relative velocity at the interfacial region to achieve an effective coupling. The overall model functionality has been thoroughly examined and applied in the highly compressible and multiscale case of a high-speed droplet impact; new experiments have been performed for a water droplet splashing on a surface at Weber number ~10^5 that have not been previously reported in the literature. The obtained results have shown a good agreement with the conducted experimental study regarding the capturing of the macroscopic characteristics of droplet fragmentation. Additionally, the proposed model has provided significant advantages particularly under a dispersed flow regime which dominates the later stages of droplet splashing in comparison to numerical methods imposing a sharpened interface and thus excluding all the relevant sub-grid scale phenomena. The developed multiscale two-fluid methodology contributes with significant additional information regarding the physical phenomenon evolution, like the relative velocity field, the shock waves development and the interface surface area evolution, which have contributed to a better understanding and more accurate modelling of complex multiscale flow fields.

Acknowledgements

The research leading to these results has received funding from the European Union's Horizon 2020 Research and Innovation programme under the Marie Skłodowska-Curie Grant Agreement No 675676.

Nomenclature

α	volume fraction [-]
C_α	interface compression coefficient [-]
C_D	drag coefficient [-]
C_{SGS}	sub-grid scale mechanisms adjustable constant coefficient [-]
d	diameter [m]
Δt	computational time step [s]
e	specific internal energy [kJ/kg]
E	interfacial energy source term [W/m^2]
F_D	drag force [N]
$F_{D\alpha}$	artificial drag force [N]
F_s	surface tension force [N]
g	acceleration of gravity [m/s^2]
k	specific kinetic energy [kJ/kg]
κ	interface curvature [1/m]
M	interfacial momentum source term [Pa/m]
ν	kinematic viscosity [m^2/s]

ν_{topo}	topological parameter [-]
Oh	Ohnesorge number [-]
p	pressure [Pa]
$\mathbf{q}^{\mathrm{eff}}$	effective heat flux vector [W/m]
$R_{\alpha l}$	turbulent liquid flux
R_{Σ}	turbulent flux of interface surface area density
Re	Reynolds number [-]
ρ	density [kg/m^3]
σ	surface tension coefficient [kg/s^2]
Sc	Schmidt number [-]
Σ	liquid gas interface surface area density [1/m]
Σ*	equilibrium liquid gas interface surface area density [1/m]
Σ_{min}	minimum liquid gas interface surface area density [1/m]
$\boldsymbol{\tau}^{\mathrm{eff}}$	effective stress tensor [Pa]
τ_r	artificial drag force relaxation factor [-]
τ_{SGS}	sub-grid scale mechanisms time scale [1/s]
u	velocity field [m/s]
u_c	artificial compression velocity field [m/s]
u_r	relative velocity field [m/s]
We	Weber number [-]
y^+	dimensionless wall distance [-]
ψ	compressibility [s/m]

Subscripts

g	gaseous phase
l	liquid phase
m	liquid and gaseous mixture
SGS	sub-grid scale component
t	turbulent component

References

Andreini, A. *et al.* (2016) 'Development of a turbulent liquid flux model for Eulerian-Eulerian multiphase flow simulations', *International Journal of Multiphase Flow*. Elsevier Ltd, 81, pp. 88–103. doi: 10.1016/j.ijmultiphaseflow.2016.02.003.

Anez, J. *et al.* (2018) 'Eulerian–Lagrangian spray atomization model coupled with interface capturing method for diesel injectors', *International Journal of Multiphase Flow*. Elsevier Ltd. doi: 10.1016/j.ijmultiphaseflow.2018.10.009.

Antonini, C., Amirfazli, A. and Marengo, M. (2012) 'Drop impact and wettability: From hydrophilic to superhydrophobic surfaces', *Physics of Fluids*, 24(10). doi: 10.1063/1.4757122.

AVL (2013) *FIRE v2013 Manuals*. Graz, Austria, AVL LIST GmbH.

Beig, S. A., Aboulhasanzadeh, B. and Johnsen, E. (2018) 'Temperatures produced by inertially collapsing bubbles near rigid surfaces', *Journal of Fluid Mechanics*, 852, pp. 105–125. doi: 10.1017/jfm.2018.525.

Berlemont, A., Desjonqueres, P. and Gouesbet, G. (1990) 'Particle lagrangian simulation in turbulent flows', *International Journal of Multiphase Flow*, 16(1), pp. 19–34. doi: 10.1016/0301-9322(90)90034-G.

Bertola, V. (2015) 'An impact regime map for water drops impacting on heated surfaces', *International Journal of Heat and Mass Transfer*. Elsevier Ltd, 85, pp. 430–437. doi: 10.1016/j.ijheatmasstransfer.2015.01.084.

Bhaga, D. and Weber, M. E. (1981) 'Bubbles in viscous liquids: shapes, wakes and velocities', *Journal of Fluid Mechanics*, 105, pp. 61–85. doi: 10.1017/S002211208100311X.

Boileau, M. *et al.* (2008) 'Investigation of Two-Fluid Methods for Large Eddy Simulation of Spray Combustion in Gas Turbines', *Flow, Turbulence and Combustion*, 80(3), pp. 291–321. doi: 10.1007/s10494-007-9123-1.

Boussinesq, J. (1877) 'Essai sur la théorie des eaux courantes', *Mémoires présentés par divers savants à l'Académie des Sciences*, 23(1), pp. 1–680.

Brackbill, J. U., Kothe, D. B. and Zemach, C. (1992) 'A Continuum Method for Modeling Surface Tension', *Journal of Computational Physics*, 100(335–354).

Černe, G., Petelin, S. and Tiselj, I. (2001) 'Coupling of the Interface Tracking and the Two-Fluid Models for the Simulation of Incompressible Two-Phase Flow', *Journal of Computational Physics*, 171(2), pp. 776–804. doi: 10.1006/jcph.2001.6810.

Chesnel, J. *et al.* (2011) 'Large Eddy Simulation of liquid jet primary breakup', *Atomization and Sprays*, 21(9), pp. 711–736.

Clift, R., Grace, J. and Weber, M. (2005) *Bubbles, drops, and particles*. Courier Corporation.

Cossali, G. E., Santini, M. and Marengo, M. (2005) 'Single-Drop Empirical Models for Spray Impact on Solid Walls: a Review', *Atomization and Sprays*, 15(6), pp. 699–736. doi: 10.1615/AtomizSpr.v15.i6.50.

Demoulin, F.-X. *et al.* (2007) 'A New Model for Turbulent Flows with Large Density Fluctuations: Application to Liquid Atomization', *Atomization and Sprays*, 17(4), pp. 315–346. doi: 10.1615/AtomizSpr.v17.i4.20.

Deshpande, S. S., Anumolu, L. and Trujillo, M. F. (2012) 'Evaluating the performance of the two-phase flow solver interFoam', *Computational Science and Discovery*, 5(1). doi: 10.1088/1749-4699/5/1/014016.

Drew, D. A. (1983) *Mathematical modeling of two-phase flow.*, *Annual Review of Fluid Mechanics*. doi: 10.1146/annurev.fl.15.010183.001401.

Dukowicz, J. (1980) 'A Particle-Fluid Numerical Model for Liquid Sprays', *Journal of Computational Physics*, 35, pp. 229–253.

Fedkiw, R. P. *et al.* (1999) 'A Non-oscillatory Eulerian Approach to Interfaces in Multimaterial Flows (the Ghost Fluid Method)', *Journal of Computational Physics, 152*(2), pp. 457–492. doi: 10.1006/jcph.1999.6236.

Field, J. E., Dear, J. P. and Ogren, J. E. (1989) 'The effects of target compliance on liquid drop impact', *Journal of Applied Physics*, 65(2), pp. 533–540. doi: 10.1063/1.343136.

García-Oliver, J. M. *et al.* (2013) 'Diesel spray CFD simulations based on the Σ-Y eulerian atomization modely', *Atomization and Sprays*, 23(1), pp. 71–95. doi: 10.1615/AtomizSpr.2013007198.

Gorokhovski, M. A. and Saveliev, V. L. (2003) 'Analyses of Kolmogorov's model of breakup and its application into Lagrangian computation of liquid sprays under air-blast atomization', *Physics of Fluids*, 15(1), pp. 184–192. doi: 10.1063/1.1527914.

Gorokhovski, M. and Herrmann, M. (2008) 'Modeling Primary Atomization', *Annual Review of Fluid*

Mechanics, 40(1), pp. 343–366. doi: 10.1146/annurev.fluid.40.111406.102200.

Guildenbecher, D. R., Lopez-Rivera, C. and Sojka, P. E. (2009) 'Secondary atomization', *Experiments in Fluids*, 46(3), pp. 371–402. doi: 10.1007/s00348-008-0593-2.

Guo, Y., Lian, Y. and Sussman, M. (2016) 'Investigation of drop impact on dry and wet surfaces with consideration of surrounding air', *Physics of Fluids*, 28(7). doi: 10.1063/1.4958694.

Haller, K. K. *et al.* (2002) 'Computational study of high-speed liquid droplet impact', *Journal of Applied Physics*, 92(5), pp. 2821–2828. doi: 10.1063/1.1495533.

Herrmann, M. (2010) 'Detailed Numerical Simulations of the Primary Atomization of a Turbulent Liquid Jet in Crossflow', *Journal of Engineering for Gas Turbines and Power*, 132(6), p. 061506. doi: 10.1115/1.4000148.

Hirt, C. W. and Nichols, B. D. (1981) 'Volume of Fluid (VOF) Method for the Dynamics of Free Boundaries', *Journal of Computational Physics*, 39, pp. 201–225.

Hysing, S. *et al.* (2009) 'Quantitative benchmark computations of two-dimensional bubble dynamics', *International Journal for Numerical Methods in Fluids*, 60, pp. 1259–1288. doi: 10.1002/fld.1934.

Ishii, M. and Hibiki, T. (2011) *Thermo-Fluid Dynamics of Two-Phase Flow*. 2nd edn. Springer-Verlag New York. doi: 10.1007/978-1-4419-7985-8.

Ishii, M. and Mishima, K. (1984) 'Two-fluid model and hydrodynamic constitutive relations', *Nuclear Engineering and Design*, 82(2–3), pp. 107–126. doi: 10.1016/0029-5493(84)90207-3.

Ishii, M. and Zuber, N. (1979) 'Drag coefficient and relative velocity in bubbly, droplet or particulate flows', *AIChE Journal*, 25(5), pp. 843–855. doi: 10.1002/aic.690250513.

Ivings, M. J., Causon, D. M. and Toro, E. F. (1998) 'On Riemann solvers for compressible liquids', *International Journal for Numerical Methods in Fluids*, 28(3), pp. 395–418. doi: 10.1002/(SICI)1097-0363(19980915)28:3<395::AID-FLD718>3.0.CO;2-S.

Jadidi, M. *et al.* (2014) 'Coupled Level Set and Volume of Fluid method in OpenFoam with application to compressible two-phase flow', in *22nd Annual Conference of the CFD Society of Canada*.

Josserand, C. and Thoroddsen, S. T. (2016) 'Drop Impact on a Solid Surface', *Annual Review of Fluid Mechanics*, 48, pp. 365–391. doi: https://doi.org/10.1146/annurev-fluid-122414-034401.

Kandlikar, S. G. and Bapat, A. V. (2007) 'Evaluation of jet impingement, spray and microchannel chip cooling options for high heat flux removal', *Heat Transfer Engineering*, 28(11), pp. 911–923. doi: 10.1080/01457630701421703.

Kelbaliyev, G. I. (2011) 'Drag Coefficients of Variously Shaped Solid Particles , Drops , and Bubbles', 45(3), pp. 248–266. doi: 10.1134/S0040579511020084.

Kolev, N. I. (2007) *Multiphase flow dynamics 2. Thermal and mechanical interactions*. 3rd edn. Springer-Verlag Berlin Heidelberg. doi: 10.1007/3-540-69835-3.

Koukouvinis, P. *et al.* (2016) 'Large Eddy Simulation of Diesel injector including cavitation effects and correlation to erosion damage', *Fuel*. Elsevier Ltd, 175, pp. 26–39. doi: 10.1016/j.fuel.2016.02.037.

Kyriazis, N., Koukouvinis, P. and Gavaises, M. (2018) 'Modelling cavitation during drop impact on solid surfaces', *Advances in Colloid and Interface Science*. Elsevier B.V., 260, pp. 46–64. doi: 10.1016/j.cis.2018.08.004.

Lahey, R. T. (2005) 'The simulation of multidimensional multiphase flows', *Nuclear Engineering and Design*, 235(10–12), pp. 1043–1060. doi: 10.1016/j.nucengdes.2005.02.020.

Lebas, R. *et al.* (2009) 'Numerical simulation of primary break-up and atomization: DNS and modelling study', *International Journal of Multiphase Flow*. Elsevier Ltd, 35(3), pp. 247–260. doi: 10.1016/j.ijmultiphaseflow.2008.11.005.

Liang, G. and Mudawar, I. (2017) 'Review of drop impact on heated walls', *International Journal of Heat and Mass Transfer*, 106, pp. 103–126. doi: 10.1016/j.ijheatmasstransfer.2016.10.031.

Ma, T. *et al.* (2017) 'A numerical study of spray/wall impingement based on droplet impact phenomenon', *International Journal of Heat and Mass Transfer*, 112, pp. 401–412. doi: 10.1016/j.ijheatmasstransfer.2017.04.110.

Malgarinos, I. *et al.* (2014) 'VOF simulations of the contact angle dynamics during the drop spreading: Standard models and a new wetting force model', *Advances in Colloid and Interface Science*. Elsevier B.V., 212, pp. 1–20. doi: 10.1016/j.cis.2014.07.004.

Marble, F. E. and Broadwell, J. E. (1977) 'The Coherent Flame Model of the Turbulent Chemical Reactions', *Acta Astronautica*, 4, pp. 291–391.

Marchisio, D. L. *et al.* (2003) 'Quadrature method of moments for population-balance equations', *AIChE Journal*, 49(5), pp. 1266–1276. doi: 10.1002/aic.690490517.

Marschall, H. (2011) *Technische Universität München Lehrstuhl I für Technische Chemie Towards the Numerical Simulation of Multi-Scale Two-Phase Flows*.

Moreira, A. L. N., Moita, A. S. and Panão, M. R. (2010) 'Advances and challenges in explaining fuel spray impingement: How much of single droplet impact research is useful?', *Progress in Energy and Combustion Science*, 36(5), pp. 554–580. doi: 10.1016/j.pecs.2010.01.002.

Mundo, C., Sommerfeld, M. and Tropea, C. (1995) 'Droplet-wall collisions: Experimental studies of the deformation and breakup process', *International Journal of Multiphase Flow*, 21(2), pp. 151–173. doi: 10.1016/0301-9322(94)00069-V.

Navarro-Martinez, S. (2014) 'Large eddy simulation of spray atomization with a probability density function method', *International Journal of Multiphase Flow*. Elsevier Ltd, 63, pp. 11–22. doi: 10.1016/j.ijmultiphaseflow.2014.02.013.

Niu, Y. Y. and Wang, H. W. (2016) 'Simulations of the shock waves and cavitation bubbles during a three-dimensional high-speed droplet impingement based on a two-fluid model', *Computers and Fluids*. Elsevier Ltd, 134–135, pp. 196–214. doi: 10.1016/j.compfluid.2016.05.018.

Osher, S. and Fedkiw, R. (2006) *Level set methods and dynamic implicit surfaces*. Vol. 153. Springer Science & Business Media.

Pan, K. L., Tseng, K. C. and Wang, C. H. (2010) 'Breakup of a droplet at high velocity impacting a solid surface', *Experiments in Fluids*, 48(1), pp. 143–156. doi: 10.1007/s00348-009-0697-3.

Pei, Y. *et al.* (2015) 'Large eddy simulation of a reacting spray flame with multiple realizations under compression ignition engine conditions.', *Combustion and Flame*, 162(12), pp. 4442–4455.

Range, K. and Feuillebois, F. (1998) 'Influence of Surface Roughness on Liquid Drop Impact', *Journal of colloid and interface science*, 203(1), pp. 16–30.

Rein, M. (1993) 'Phenomena of liquid drop impact on solid and liquid surfaces', *Fluid Dynamics Research*, 12(2), pp. 61–93. doi: 10.1016/0169-5983(93)90106-K.

Roisman, I. V., Lembach, A. and Tropea, C. (2015) 'Drop splashing induced by target roughness and porosity: The size plays no role', *Advances in Colloid and Interface Science*. Elsevier B.V., 222, pp. 615–621. doi: 10.1016/j.cis.2015.02.004.

Rossinelli, D. *et al.* (2013) '11 PFLOP/s simulations of cloud cavitation collapse', in *Proceedings of the International Conference on High Performance Computing, Networking, Storage and Analysis*, pp. 1–13. doi: 10.1145/2503210.2504565.

Rusche, H. (2002) *Computational Fluid Dynamics of Dispersed Two-Phase Flows at High Phase Fractions*, *PhD Thesis*. doi: 10.1145/1806799.1806850.

Saurel, R., Petitpas, F. and Abgrall, R. (2008) *Modelling phase transition in metastable liquids: application to cavitating and flashing flows*, *Journal of Fluid Mechanics*. doi: 10.1017/S0022112008002061.

Scardovelli, R. and Zaleski, S. (1999) 'Direct numerical simulation of free-surface and interfacial flow', *Annual Review of Fluid Mechanics*, 31(1), pp. 567–603.

Schiller, L. and Naumann, A. Z. (1933) 'Über die grundlegenden Berechnungen bei der Schwerkraftaufbereitung', *Ver. Deut. Ing.*, 77(12), pp. 318–320.

Schügerl, K. and Bellgardt, K.-H. (2000) *Bioreaction engineering: modeling and control.* 1st edn. Springer-Verlag Berlin Heidelberg. doi: 10.1007/978-3-642-59735-0.

Sethian, J. A. (1996) 'A fast marching level set method for monotonically advancing fronts.', *Proceedings of the National Academy of Sciences*, 93(4), pp. 1591–1595. doi: 10.1073/pnas.93.4.1591.

Sharp, D. H. (1983) 'An Overview of Rayleigh-Taylor Instability', in *International conference on "Fronts, Interfaces and Patterns"*.

Shinjo, J. and Umemura, A. (2010) 'Simulation of liquid jet primary breakup: Dynamics of ligament and droplet formation', *International Journal of Multiphase Flow*. Elsevier Ltd, 36(7), pp. 513–532. doi: 10.1016/j.ijmultiphaseflow.2010.03.008.

Shinjo, J. and Umemura, A. (2011) 'Surface instability and primary atomization characteristics of straight liquid jet sprays', *International Journal of Multiphase Flow*. Elsevier Ltd, 37(10), pp. 1294–1304. doi: 10.1016/j.ijmultiphaseflow.2011.08.002.

Shonibare, O. Y. and Wardle, K. E. (2015) 'Numerical investigation of vertical plunging jet using a hybrid multifluid-VOF multiphase CFD solver', *International Journal of Chemical Engineering*, 2015. doi: 10.1155/2015/925639.

Strubelj, L. and Tiselj, I. (2011) 'Two-fluid model with interface sharpening', *International Journal for Numerical Methods in Engineering*, 85, pp. 575–590.

Štrubelj, L., Tiselj, I. and Mavko, B. (2009) 'Simulations of free surface flows with implementation of surface tension and interface sharpening in the two-fluid model', *International Journal of Heat and Fluid Flow*. Elsevier Inc., 30(4), pp. 741–750. doi: 10.1016/j.ijheatfluidflow.2009.02.009.

Theofanous, T. G. (2011) 'Aerobreakup of Newtonian and Viscoelastic Liquids', *Annual Review of Fluid Mechanics*, 43(1), pp. 661–690. doi: 10.1146/annurev-fluid-122109-160638.

Thoroddsen, S. T., Etoh, T. G. and Takehara, K. (2008) 'High-Speed Imaging of Drops and Bubbles', *Annual Review of Fluid Mechanics*, 40(1), pp. 257–285. doi: 10.1146/annurev.fluid.40.111406.102215.

Thoroddsen, S. T., Takehara, K. and Etoh, T. G. (2012) 'Micro-splashing by drop impacts', *Journal of Fluid Mechanics*, 706, pp. 560–570. doi: 10.1017/jfm.2012.281.

Tomiyama, A. *et al.* (2002) 'Terminal velocity of single bubbles in surface tension force dominant regime', *International Journal of Multiphase Flow*, 28(9), pp. 1497–1519. doi: 10.1016/S0301-

9322(02)00032-0.

Tomiyama, A. and Shimada, N. (2001) 'A numerical method for bubbly flow simulation based on a multi-fluid model', *Journal of pressure vessel technology*, 123(4), pp. 510–516.

Tryggvason, G. *et al.* (2002) 'A Front-Tracking Method for the Computations of Multiphase Flow', *Journal of Computational Physics*, 169(2), pp. 708–759. doi: 10.1006/jcph.2001.6726.

Unverdi, S. O. and Tryggvason, G. (1992) 'A front-tracking method for viscous, incompressible, multi-fluid flows', *Journal of Computational Physics*, 100(1), pp. 25–37. doi: 10.1016/0021-9991(92)90307-K.

Vallet, A. and Borghi, R. (1999) 'Modelisation eulerienne de l'atomisation d'un jet liquide', pp. 1015–1020.

Vallet, A., Burluka, A. A. and Borghi, R. (2001) 'Development of a Eulerian model for the "atomization" of a liquid jet', *Atomization and sprays*, 11(6).

Visser, C. W. *et al.* (2012) 'Microdroplet impact at very high velocity', *Soft Matter*, 8(41), pp. 10732–10737. doi: 10.1039/c2sm26323h.

Visser, C. W. *et al.* (2015) 'Dynamics of high-speed micro-drop impact: Numerical simulations and experiments at frame-to-frame times below 100 ns', *Soft Matter*. Royal Society of Chemistry, 11(9), pp. 1708–1722. doi: 10.1039/c4sm02474e.

Vujanović, M. *et al.* (2015) 'Numerical modelling of diesel spray using the Eulerian multiphase approach', *Energy Conversion and Management*, 104, pp. 160–169. doi: 10.1016/j.enconman.2015.03.040.

Wardle, K. E. and Weller, H. G. (2013) 'Hybrid multiphase CFD solver for coupled dispersed/segregated flows in liquid-liquid extraction', *International Journal of Chemical Engineering*, 2013(1). doi: 10.1155/2013/128936.

Worthington, A. M. (1877) 'XXVIII. On the forms assumed by drops of liquids falling vertically on a horizontal plate', *Proceedings of the royal society of London*, 25(171–178), pp. 261–272.

Wu, W., Xiang, G. and Wang, B. (2018) 'On high-speed impingement of cylindrical droplets upon solid wall considering cavitation effects', *Journal of Fluid Mechanics*, 857, pp. 851–877. doi: 10.1017/jfm.2018.753.

Wu, Z. and Cao, Y. (2017) 'Dynamics of initial drop splashing on a dry smooth surface', pp. 1–11.

Xu, L., Zhang, W. W. and Nagel, S. R. (2005) 'Drop splashing on a dry smooth surface', *Physical Review Letters*, 94(18), pp. 1–4. doi: 10.1103/PhysRevLett.94.184505.

Yarin, A. L. (2006) 'DROP IMPACT DYNAMICS: Splashing, Spreading, Receding, Bouncing…', *Annual Review of Fluid Mechanics*, 38(1), pp. 159–192. doi: 10.1146/annurev.fluid.38.050304.092144.

Yarin, A. L. and Weiss, D. A. (1995) 'Impact of Drops on Solid Surfaces: Self-Similar Capillary Waves, and Splashing as a New Type of Kinematic Discontinuity', *Journal of Fluid Mechanics*, 283, pp. 141–173. doi: 10.1017/S0022112095002266.